Materials Today Chemistry 35 (2024) 101910

Contents lists available at ScienceDirect

Materials Today Chemistry

journal homepage: www.journals.elsevier.com/materials-today-chemistry/

How defects in lanthanum iron manganite perovskite structures promote the catalytic reduction of NO by CO

Asghar Mohammadi [a], Christoph W. Thurner [a], Leander Haug [a], Maged F. Bekheet [b], Julian T. Müller [b], Aleksander Gurlo [b], Clivia Hejny [c], Parastoo Delir Kheyrollahi Nezhad [a], Daniel Winkler [a], Wiebke Riedel [d], Simon Penner [a,*]

[a] Institute of Physical Chemistry, University of Innsbruck, Innrain 52c, A-6020, Innsbruck, Austria
[b] Technische Universität Berlin, Faculty III Process Sciences, Institute of Materials Science and Technology, Chair of Advanced Ceramic Materials, Straße des 17. Juni 135, 10623, Berlin, Germany
[c] Institute of Mineralogy and Petrography, University of Innsbruck, Innrain 52d, A-6020, Innsbruck, Austria
[d] Institut für Chemie, Freie Universität Berlin, Arnimallee 22, 14195, Berlin, Germany

ARTICLE INFO

Keywords:
In situ X-ray photoelectron spectroscopy
In situ X-ray diffraction
Defects
Nitrogen oxide abatement

ABSTRACT

Adjusting the defect level during synthesis of A- and B-site deficient lanthanum iron manganite (LFM) perovskites shows that non-stoichiometry can beneficially influence the catalytic reactivity to N_2 in the reduction of NO by CO on noble metal-free LFM-based perovskites. Optimal steering of La deficiency and the associated redox chemistry to reduce the near-surface regions during catalytic operation at low temperatures is the key factor. Surface enrichment by reducible B site cations and a proper design of structural defects resulting from the optimum introduction of La defects exclusively cause in-situ reduction of surface-near regions by CO oxidation, as well as formation of oxygen vacancies for enhanced NO and N_2O reactivity. Excess doping with defects causes structural instability and continuous supply of oxygen from the catalyst bulk to the surface at elevated temperatures. Introduction of B site vacancies leads to surface enrichment by non-reducible lanthanum cations, causing suppressed catalyst activity undercutting even stoichiometric LFM.

1. Introduction

The outlet exhaust stream of motor vehicles with hydrocarbon-based fuels consists of varied compositions of NO_x, CO, as well as unburned hydrocarbons, and is extremely harmful to both environment and human life [1–4]. Reduction of NO by CO is an important reaction in three-way catalysis (TWC), as it predominantly contributes to the removal of nitrogen oxides [5–8]. TWCs typically contain Pt, Pd (for oxidation of CO and hydrocarbons), as well as Rh (for the reductive conversion of NO_x) - due to economic reasons, alternative catalyst materials with reduced noble metal content are highly requested [7,9].

Materials that have been shown to be capable of replacing noble metals in such reactions are perovskites. Oxides with perovskite structure (with the general formula ABO_3) have important applications in many research areas, especially heterogeneous catalysis, electrocatalysis, photocatalysis, and as energy storage materials. The unique ability of these structures to incorporate a variety of polyvalent metal ions is the most important aspect from a structural and chemical point of view [10]. Variation in the metal oxidation state and a considerable tolerance in the anionic sub-lattice vacancies under different atmospheres, upon aliovalent substitution or under non-stoichiometric synthesis conditions, impacts the electronic and catalytic properties of the perovskites [10–12]. As a consequence, the knowledge-based design and modification of these materials can be implemented by tuning the defect chemistry [13]. The latter is directly related to the stoichiometry of the materials and, as such, to the oxidation states of the transition metal cations [14]. Clarifying the relationship between the stoichiometry and chemistry steered by the synthesis conditions and the resulting defect chemistry of the perovskite materials is of high interest as the catalytic activity of these materials can be governed for different applications. Among (non-) stoichiometric perovskites with different compositions and applications, $LaNi_{0.5}Ti_{0.5}O_3$ [15], $La_{2-x}CoTiO_{6-\delta}$ [10], La_xMnO_3 [16], $LaMn_{0.9}O_3$ [17], $La_{0.7}MnO_{3-\delta}$ [18] and $La_{1-x}Fe_yMn_{1-y}O_3$ [12] attracted considerable interest. Compared to the parent stoichiometric

* Corresponding author.
E-mail address: simon.penner@uibk.ac.at (S. Penner).

https://doi.org/10.1016/j.mtchem.2024.101910
Received 25 October 2023; Received in revised form 12 December 2023; Accepted 5 January 2024
Available online 9 January 2024

$LaMnO_3$ perovskite, the nonstoichiometric counterparts exhibit specific beneficial structural and electronic properties, such as a change in Mn^{4+}/Mn^{3+} ratio [19], active oxygen mobility [17] and ionic vacancy defect concentration [20,21].

For the NO reduction by CO, La-based perovskites were frequently used in previous research [2,7,22–28]. Ferrite and manganite-based perovskites serve as important model perovskites in this respect, as they allow to study the effect of the redox couples Mn^{4+}/Mn^{3+} and Fe^{4+}/Fe^{3+} on NO reactivity, and especially iron-containing perovskites show high thermal stability and catalyst lifetime [12,29]. Wu et al. recently provided a detailed overview of the importance of ferrite- and manganite-based perovskites in deNOx applications and, in due course, also reported an improved performance of $La_{0.7}Fe_{0.8}Mn_{0.2}O_{3-x}$ materials under automotive three-way conditions, governed by the coupling of the Mn^{3+}/Mn^{4+} ratio to A-site La deficiency [12]. Despite the highlighted importance of the defects, it also features the still missing in situ characterization and does not take into account the defect chemistry changes directly under operational conditions. An important aspect of our work is, therefore, to show that despite the possibility of synthesizing defective $La_xFe_{0.7}Mn_{0.3}O_{3-\delta}$ - based perovskites, they are prone to suffer from different bulk structural and surface-chemical changes (i.e., exsolution of iron and manganese as a function of the degree of non-stoichiometry) during catalytic operation of the reduction of NO by CO. The reduction of NO by CO is especially suited for this purpose: it is a redox reaction, and the reaction mechanism is reported to be mediated by oxygen vacancies in metal oxides following the Mars-van Krevelen mechanism [8,30]. The created oxygen vacancies facilitate NO (and N_2O) reduction following CO oxidation to CO_2, and replenishment with O atoms resulting from NO dissociation closes the reaction cycle. As non-stoichiometric materials are known to more easily release lattice oxygen, thus, becoming more active than their stoichiometric counterparts [17], we expect that the introduction of defects into selected manganite-based perovskite structures and their reactivity have a beneficial impact on the activity and selectivity in the NO + CO reaction. The latter is especially important, as intermediary-formed N_2O is a 300 times more powerful greenhouse gas than CO_2, causing ozone depletion, acid rain formation and photochemical smog [31]. In our previous work, we have already shown that oxygen vacancies in LFM-based perovskites are active for the decomposition of N_2O [2]. In a similar line of argumentation, Cho et al. reported that oxygen vacancies work as catalytically active sites for N_2O adsorption and decomposition [32].

The present work focuses on a comparative approach of assessing the NO + CO reactivity of different A- and B-site deficient perovskite materials ($La_xFe_{0.7}Mn_{0.3}O_3$, x = 0.85 and 0.70; $La(Fe_{0.7}Mn_{0.3})_yO_3$, y = 0.85) derived from the parent $LaMnO_3$ perovskite structure, which has already been shown to be a promising material for the catalytic reduction of NO by CO [2,12,33]. Steering of the defect chemistry eventually allows us to improve the catalytic activity and N_2 selectivity and identify beneficial and detrimental parameters for activity/selectivity steering. The main goal of this work is the experimental proof of actively and beneficially manipulating the oxidation state of the B site cations, the correlated concentration of defects at the A site and the associated oxygen content of perovskites for improving the activity of NO reduction by CO. An important aspect of this work is the economization of the noble metals usually present in perovskite materials for $deNO_x$ applications. As we have evidenced for similar Cu- and Pd-containing perovskites in the NO + CO reaction, manipulating the composition of the perovskites allows for steering of the (noble) metal-perovskite interface and, in due course, to economize the use of the noble metal [2,26,28]. In a similar line of argumentation, we now strive to assess the possibility to completely compensate the use of a noble metal by La deficiency steering in terms of NO activity and N_2 selectivity. A guiding principle of our work in this respect is the authoritative use of in situ structural and chemical characterization tools, such as in situ X-ray diffraction and in situ X-ray photoelectron spectroscopy, to combine bulk and surface-limited information to obtain a complete picture of catalytic action and mechanistic details.

2. Experimental

2.1. Preparation of the materials

A sol-gel synthesis approach using the metal nitrate precursor materials $La(NO_3)_3{\cdot}6H_2O$, $Mn(NO_3)_2{\cdot}4H_2O$ and $Fe(NO_3)_3{\cdot}9H_2O$ was followed for the preparation of the stoichiometric and non-stoichiometric lanthanum iron manganite (LFM) samples. Details of the synthesis routine are outlined in Ref. [2]. A final calcination step for 5 h at 700 °C yielded the starting materials, which were characterized by ex-situ XRD to verify successful synthesis. Table 1 gives an overview of the nominal compositions and the acronyms used. We will use the term "stoichiometric" from now on for the reference LFM catalyst, although ICP analysis reveals a slight deviation from the ideal $LaMnO_3$ stoichiometry to set LFM apart from the samples with deliberate and controlled non-stoichiometry.

2.2. Chemical and structural characterization

Elemental analyses for lanthanum (La), iron (Fe) and manganese (Mn) were performed with inductively coupled plasma optical emission spectroscopy (ICP-OES) by using a Horiba Scientific ICP Ultima 2 (Horiba, Kyoto, Japan). Prior to analysis, powder samples were digested in an aqueous suspension of HNO_3 and HF acid mixture at 200 °C for 5 h in a Teflon-lined autoclave.

BET-based specific surface areas were measured by means of nitrogen sorption, using a Quanta- Chrome Nova 2000e surface and pore size analyzer and liquid N_2 as adsorbent. Before testing, the samples were degassed at 270 °C in vacuo for 1 h.

Ex-situ X-ray diffraction data were collected using a STOE STADI X-ray powder diffractometer in transmission geometry and Mo Kα1 radiation (λ = 0.7093 Å) using a focusing Ge(111) primary beam monochromator, as well as a MYTHEN 1 K linear position-sensitive detector system. Structure analysis was performed based on the references from the Crystallography Open Database (COD) using the FULLPROF software tool.

In situ synchrotron X-ray diffraction experiments have been conducted in NO + CO mixtures at the beamline 12.2.2, Advanced Light Source (ALS) at Berkeley National Laboratory. The diffraction patterns were measured in angle-dispersive transmission mode with a focused 25 keV monochromatic beam (λ = 0.4984 Å/30 μm spot size). The powders were heated in a 0.7 mm outer diameter quartz capillary under quasi-flowing conditions (hydrogen, oxygen or dry and humid NO + CO = 1:1 reaction mixtures). The gases were injected through a 0.5 mm outer diameter tungsten tube. Heating was performed using a SiC furnace with an infrared light source up to 700 °C at a rate of 10 °C min^{-1}. The XRD patterns were recorded by a PerkinElmer flat panel detector (XRD 1621, dark image, and strain correction) [34,35]. Rietveld refinement was performed using the FULLPROF program [36]. The profile function 7 (Thompson–Cox–Hastings pseudo-Voigt convoluted with axial divergence asymmetry function) was used in all refinements. The resolution function of the diffractometers was obtained from the structure refinement of a LaB_6 standard.

For the stoichiometric LFM catalyst, X-ray powder diffraction patterns at elevated temperatures were recorded using a Rigaku SmartLab-3kW instrument in parallel beam setting and reflection mode (Cu-Kα, λ = 1.5406 Å) using a HyPix3000 detector (Rigaku, Tokyo, Japan). The ground sample was placed on a quartz-sample holder for use in a Rigaku Reactor-X high-temperature reaction chamber used for heating. The XRD patterns were recorded in a range of 2θ 10°–90° with a step width of 0.01°. The temperature was increased by 10 °C min^{-1} and held for 1 min before each measurement. XRD patterns were recorded in 50 °C steps up to 700 °C, with a measurement in the end at 25 °C after re-cooling.

Table 1
Overview of nominal catalyst composition, BET-based specific surface area (SSA) and composition derived from ICP and ex-situ XPS analysis.

Nominal Composition	Acronyms	SSA/m^2gr^{-1}	Chemical composition based on ICP	Chemical composition based on XPS
$LaFe_{0.7}Mn_{0.3}O_3$	LFM	12.4	$La_{1.07}Fe_{0.67}Mn_{0.26}O_{3-\delta}$	$La_{1.55}Fe_{0.22}Mn_{0.13}O_{3-\delta}$
$La_{0.85}Fe_{0.7}Mn_{0.3}O_3$	$L_{0.85}FM$	25.0	$La_{0.94}Fe_{0.66}Mn_{0.26}O_{3-\delta}$	$La_{1.20}Fe_{0.33}Mn_{0.16}O_{3-\delta}$
$La_{0.7}Fe_{0.7}Mn_{0.3}O_3$	$L_{0.7}FM$	32.0	$La_{0.78}Fe_{0.66}Mn_{0.26}O_{3-\delta}$	$La_{0.90}Fe_{0.43}Mn_{0.18}O_{3-\delta}$
$LaFe_{0.6}Mn_{0.25}O_3$	$L(FM)_{0.85}$	19.5	$La_{1.09}Fe_{0.55}Mn_{0.21}O_{3-\delta}$	$La_{1.66}Fe_{0.13}Mn_{0.08}O_{3-\delta}$

2.3. Volumetric adsorption techniques

An all-quartz tubular reactor (volume 34.5 mL) was used for temperature-programmed reduction and oxidation measurements (flowing O_2 treatment, H_2-TPR, O_2-TPO). In each experimental sequence, a defined amount of about 50 mg of the powder sample was fixed by quartz wool in the reactor in a chemically inert environment. Catalysts are pretreated in flowing dry O_2 for 1 h at 700 °C and subsequently cooled down in O_2 atmosphere. In order to desorb surface- and physically-adsorbed oxygen, samples are evacuated up to a defined base pressure of 10^{-6} mbar. During the temperature-programmed hydrogen reduction (H_2-TPR) and also O_2-TPO, a defined (ca. 490 mbar) amount of pre-dried H_2 (or O_2) (using liquid N_2 cooling trap and its mixture with ethanol for O_2) was expanded from a separately calibrated volume into the entire reactor volume. After equilibration of the final reactor pressure, the temperature program was started to measure the H_2 (or O_2) uptake up to 700 °C. The temperature program included a heating phase from RT to 700 °C at a rate of 10 °C min^{-1}, followed by an isothermal period at 700 °C for 10 min, and finally, a cooling process to room temperature (rate 10 °C min^{-1}). Moisture produced from the sample during H_2-TPR was removed using a degassed zeolite as water trap installed outside of the heated reaction zone (i.e., sample and zeolite can be heated separately). A Linn High-Term tube furnace was used for heating the sample. The temperature is measured by a Ni/NiCr thermocouple placed near the sample. The pressure in the reactor system was measured using a differential Baratron® pressure transducer (MKS Instruments). Based on the H_2 (or O_2) pressure drop in the reactor system during the temperature program, the H_2 uptake could be calculated at each temperature based on the initially introduced H_2 molar amount and the ideal gas law. The effective volume of the reactor tube was determined using inert gas (He) calibration. The detailed procedure is described in Ref. [2].

2.4. Surface-chemical characterization using X-ray photoelectron spectroscopy

To elucidate the sample's surface electronic structure in situ, experiments in a customized commercial UHV system for NAP-XPS applications (SPECS GmbH) were carried out. The UHV chamber is comprised of a μFOCUS 600 NAP monochromatic small spot (100 × 300 μm^2) Al Kα X-ray source, a hemispherical energy analyzer (PHOBIOS 150 NAP) in a vertical configuration, and a μ-metal analyzing chamber, which shields the system from external magnetic fields. The differentially pumped energy analyzer allows backfilling of the analysis chamber to pressures up to 30 mbar with different gases and gas mixtures (e.g., NO + CO) via mass flow controllers (Bronkhorst). To investigate the powdered samples, a pressed pellet covering a stainless steel grid as a stabilizer is fixed on a sample holder by mounting the pellet via a front plate. An IR laser (IPG PHOTONICS, 100 W max. power) is attached to the bottom side of the analyzing chamber and allows us to heat the samples from the back side via an 8 mm hole in the sample holder. The temperature is controlled by a K-type thermocouple fixed on the stainless steel grid inside the pellet. During all experiments, an atmosphere consisting of NO and CO in a ratio 1:1 was utilized. CO (from Messer) and NO (from Linde) were used in purities of 4.7 and 2.5, respectively. The exited photoelectrons were collected by a 300 μm nozzle directly from the sample's frontside surface via an 8 mm opening in the front plate. Due to pressures in the mbar regime, the X-ray ionized gas region between the nozzle and the sample compensates charging, thus, a core-level shift can be neglected even on poorly conducting samples. The X-ray source power was set to 70 W and 13 kV, and all spectra were recorded under the exactly same conditions, especially regarding the pass energy settings (50 eV). Charging effects were accounted for by calibration of the binding energies to the C–C component of the C 1s peak (adventitious carbon) at 284.8 eV. Evaluation of the data was performed using the CasaXPS software. For calculation of the surface ion concentration, relative sensitivity factor (RSF) and electron mean free path corrections have been applied. The following relative sensitivity factors values (from the CasaXPS software) have been used: La 3d 47.6, Mn 2p 13.9, Fe 2p 16.4 and O 1s 2.93. A pass energy of 50 eV was used for all experiments.

During peak fitting of each spectrum, the lowest number of physicochemically meaningful peaks in the fitting process, reproducing the experimental data, was applied. A Shirley-type background was used for baseline correction. The fitting of the Fe $2p_{3/2}$ and Mn $2p_{3/2}$ peaks was performed in accordance with literature reports on similar perovskite materials [37–41]. Peaks were fitted by mixtures of Gaussian and Lorentzian functions (30 % Lorentzian character) as peak shapes for each component, with relevant BE's references taken from literature for each oxidation state. To converge the fitting procedure, the BE's were fixed, but the full-width-at-half-maximum (FWHM's) of the relevant peaks allowed to adjust in a narrow width regime (between 1.9 eV and 2.6 eV for the O 1s components and between 3.5 eV and 4.5 eV for the Fe 2p and Mn 2p components).

2.5. Magnetic resonance measurements

Room temperature continuous wave (cw) magnetic resonance measurements at X-band frequencies (9.86 GHz) were conducted with a Bruker B-ER420 spectrometer upgraded with a Bruker ECS 041XG microwave (mw) bridge and a lock-in amplifier (Bruker ER023 M) using a Bruker SHQ resonator applying a modulation frequency of 100 kHz. All measurements were conducted with a modulation amplitude of 0.5 mT, a modulation frequency of 100 kHz and 20 dB mw attenuation. The samples were measured in quartz tubes of 2.9 mm outer diameter with a filling height of approx. 10 mm. The spectra were normalized to the sample mass in the quartz tube.

2.6. Catalytic testing in the reduction of NO by CO under dry and moist reaction conditions

200 mg of catalyst powder was fixed with quartz wool in a homebuilt 8 mm (inner diameter) quartz fixed-bed flow reactor setup under atmospheric pressure and a total flow rate of 200 mL min^{-1} (reactant composition: CO: NO: He = 1:1:98 mL min^{-1} under dry conditions; reactant composition: CO: NO: H_2O:He = 1:1:2.5:95.5 mL min^{-1} under wet conditions; GHSV = 9000 h^{-1}). In each catalytic test, the reactor was heated in a Linn High Therm tubular furnace at 2 °C min^{-1} to 550 °C followed by an isothermal period at 550 °C for 30 min H_2O in the reactor inlet was supplied by passing He stream through a water bubbler. The output gas was directly detected by both infrared spectroscopy of the gas phase (using an Agilent Cary 660 FT-IR spectrometer) and mass spectrometry (using a Balzers QME 125 quadrupol mass spectrometer). N_2 formation rates were determined by difference from the measured rates

of NO conversion and of N_2O and NH_3 formation (by infrared spectroscopy). To display the catalytic activity as a function of temperature, we use the following equation to calculate the NO conversion:

$$NO_{Conversion} = 100 * \left(1 - \frac{[NO]_{out}}{[NO]_{in}}\right)$$

$[NO]_{out}$ and $[NO]_{in}$ indicate the inlet and outlet concentration of NO, respectively.

The impact of mass transport limitations in the chosen reactor setup has been thoroughly assessed and found to be negligible. For details of calculation we refer to our previous work [2].

Catalytic data were converted from IR and mass spectrometry raw intensity data to concentration by external calibration with the respective gas mixtures To transform the temperature-dependent conversion data into turnover frequencies (TOFs), the number of active sites needs to be assessed. Dividing the respective perovskite's density by the molar mass of one perovskite formula unit yields the number of units cm^{-3}. Using an orthorhombic unit cell, the average number of units $area^{-1}$ is estimated. Correction for the total surface area of the investigated catalyst mass as derived from the BET-derived mass-specific surface area yields the number of units on the respective catalyst amount surface. This number is directly utilized as the number of active sites on the perovskite surface. The educt gas flow is obtained on the basis of the reactant concentration. The total flow can be converted to reactant/product molecules s^{-1} passing through the catalyst bed by applying the ideal gas equation (using atmospheric pressure and the average gas temperature). Finally, the TOF is obtained by division of this particle flow by the total number of active sites and multiplication with the conversion (see equation (2)). Subsequently, the TOF is plotted *vs.* the temperature.

$$N_{s,p} = \left(\frac{\rho . N_A}{M}\right)^{\frac{2}{3}} \bullet S_s \bullet m \quad (1)$$

$$\mathrm{TOF} = c \bullet 10^{-6} \bullet v \bullet \frac{p \bullet N_A}{R \bullet T_a} \bullet \frac{X}{N_{s,p}} \quad (2)$$

$N_{s,p}$ Total number of active sites of the perovskite
ρ Density of the perovskite/kg $m.^{-3}$
M Molar mass of the perovskite/kg $mol.^{-1}$
N_A Avogadro's number; 6.022 10^{23} mol^{-1}
S_s Specific surface area from BET/m^2 $kg.^{-1}$
m Sample mass/kg
TOF Turnover frequency/$s.^{-1}$
c Concentration of the gas in the educt stream/ppm
v Total gas flow/m^3 $s.^{-1}$
p Standard pressure; 101,325 Pa
R Ideal gas constant; 8.3144598 J mol^{-1} $K.^{-1}$
T_a Average gas temperature; 548 K
X Educt conversion

2.7. CO-TPR experiments in the flow reactor setup

The experimental conditions for this tests are exactly similar to the catalytic activity test conditions (section 2.6), with the difference that instead of NO, additional He flow is used to a provide total flow rate of 200 mL min^{-1} (CO: He = 1:99 mL min^{-1}).

3. Results and discussion

3.1. Structural and chemical characterization of the effects of defects in the initial materials

To determine the effect of nonstoichiometry on the specific surface area, BET characterization has been carried out (Table 1). In essence, the introduction of non-stoichiometry at the A or B site has a considerable effect on the specific surface. These results are in accordance with XRD (Fig. 1 and Table 2), where the reference LFM perovskite exhibits larger crystallites.

X-ray diffraction analysis of the materials after initial calcination (Fig. 1 (left)) verifies a single orthorhombic perovskite phase for all samples without secondary Fe/Mn - or La-oxides. Referenced to LFM, the only visible change is a slight shift of the XRD peaks to larger 2θ with peak broadening, which is most prominent in $L_{0.7}$FM (Fig. 1, right). The observed peak shift of the most intense reflection of orthorhombic LFM 112 of 0.17° 2θ is in good agreement with the difference of the calculated peak position between LFM and $L_{0.7}$FM.

To verify the nominal bulk composition, the metal content of the perovskites based on ICP analysis is also shown in Table 1. To easily compare the surface composition of the catalysts, high-resolution spectra of the La 3d, O 1s, Mn 2p and Fe 2p regions are depicted in Fig. S1, panels A–D, respectively, and quantitatively summarized in Table 1 as surface-chemical compositions. Comparison of the nominal composition of the samples with those derived from ICP and XPS data shows that the metal content in the bulk of the samples is close to the nominal ones, while a clear enrichment in La at the surface is observed for all samples. The results indicate that the intensity of the peaks related to the A or B site cations changes accordingly with the nominal synthesis composition. Changes in the Fe 2p spectra between the different perovskite samples are thereby more prominent compared to Mn 2p. Surface enrichment of perovskites with A-site cations is a well documented phenomenon [42–47], and as will be outlined in the catalytic section, it can negatively affect the catalytic activity if it is in excess. As expected, surface enrichment by La is suppressed for the La-deficient catalysts. The characteristic satellite peak for Fe (III) components is clearly visible for pure LFM and $L_{0.85}$FM, but gets gradually diminished for higher La deficiencies and the B-site deficient perovskite. The O 1s region indicates the expected three oxygen components, i.e., lattice oxygen, oxygenate-related oxygen and oxygen from adsorbed species like water or hydroxyl from low to high binding energy [2,48,49]. The relative intensity contribution of the three components is different for pure LFM and the respective A- and B-site deficient LFM materials. At least a clear trend in the reduced intensity of the components at higher binding energies with increasing La deficiency is evident. Although the concentration of oxygen vacancies and therefore, also the oxidation state of metal cations are very different within the bulk and at the surface of catalysts [50–52], according to the combined bulk and surface chemical analysis, the catalyst's composition changes in agreement with the nominal composition.

For further characterization of the defects in the different samples, cw magnetic resonance measurements were conducted (Fig. 2). All spectra display a very broad signal (ΔBpp ≈ 100 mT) which differs significantly in intensity and resonance position for the different samples. No indication for individual, paramagnetic defects including isolated, paramagnetic oxygen vacancies is found. The results are rather compatible with a strongly coupled spin system, accordingly the signal is attributed to a ferromagnetic resonance. As the magnetization depends on the Curie temperature T_C, initial magnetization measurements were conducted indicating $T_C > 130$ °C (which is above the accessible temperature range of the instrument). Thus, while an absolute quantification requires additional measurements, qualitatively, the signal intensity increases with increasing charge deficiency on the La-site, i.e., $La(FM)_{0.85} \leq LFM < La_{0.85}FM < La_{0.7}FM$. Although a clear assignment of the species is not possible based on magnetic measurements alone, we relate the signals to according changes in the Mn oxidation state, as discussed in detail below. Importantly, the results show that La defect formation is accompanied by clear changes in the magnetic properties.

3.2. Effect of La deficiency on the catalytic activity and selectivity in the reduction of NO by CO

Activity tests in the NO reduction by CO under dry conditions are

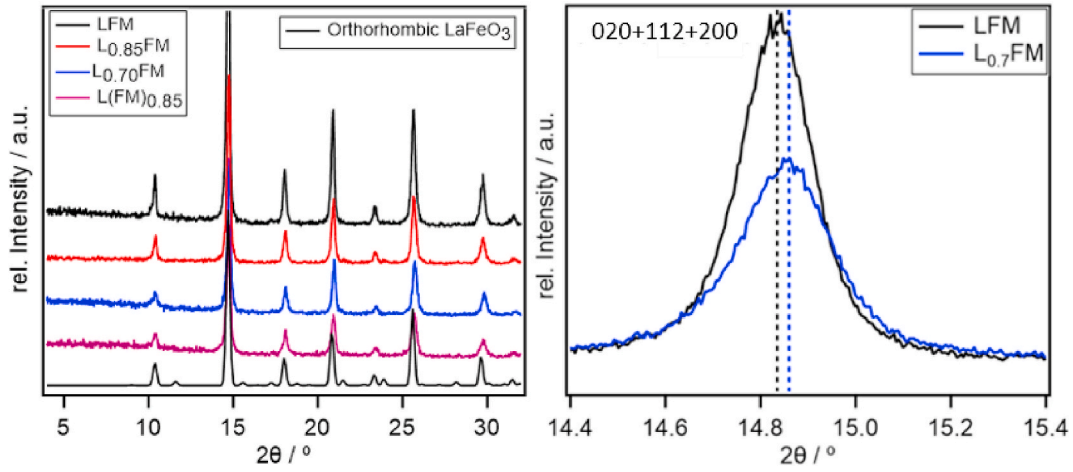

Fig. 1. XRD patterns of the pure and La-deficient LFM catalysts after initial calcination at T = 700 °C in air (left). The references used for structure and phase assignment are taken from the COD database and are related to the parent orthorhombic $LaFeO_3$ reference structure. The representative highlighted shift of the XRD pattern of $L_{0.7}FM$ referenced to stoichiometric LFM for the combined 020 + 112+200 reflex as a consequence of non-stoichiometry is shown in the right panel.

Table 2
Crystallite size, cell parameters and cell volume of catalysts derived from Rietveld refinement of the ex-situ XRD data.

Sample	Crystallite size (nm)	Cell parameter(Å)	Cell Volume(Å^3)
LFM	21.6 ± 1	a = 5.5037(6) b = 5.5475(6) c = 7.7886(9)	237.80(4)
$L_{0.85}FM$	20.6 ± 1	a = 5.5021(4) b = 5.5508(4) c = 7.7887(7)	237.87(6)
$L_{0.7}FM$	18.5 ± 1	a = 5.4954(9) b = 5.5498(9) c = 7.7829(9)	237.37(3)
$L(FM)_{0.85}$	15.2 ± 1	a = 5.4953(9) b = 5.5483(9) c = 7.7936(9)	237.62(8)

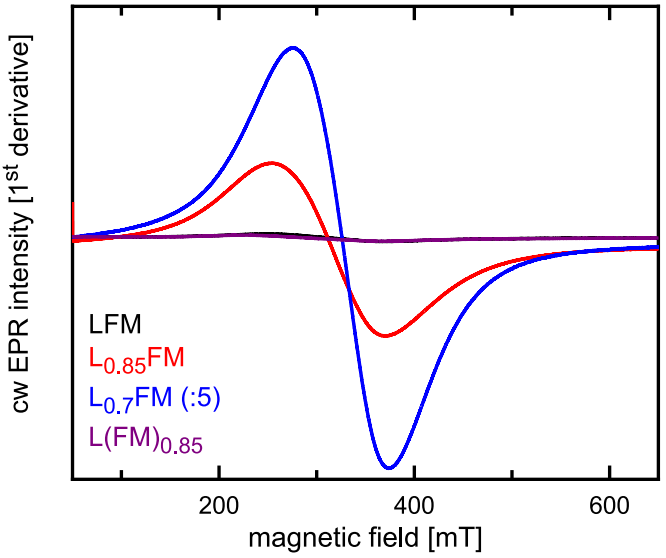

Fig. 2. Room temperature cw magnetic resonance spectra of the different LFM samples. All spectra are normalized to the sample mass. The spectrum of $L_{0.7}FM$ was scaled down (factor of 5) for better visibility.

shown in Fig. 3, Panels A and B based on NO conversion and turnover frequency (TOF) of NO molecules, respectively. The distribution of reaction products is shown in Fig. 4. Compared to the stoichiometric LFM perovskite, La deficiency enhances the catalytic activity by shifting the light-off temperature to about 50 °C lower reaction temperatures. In contrast, deficiency at the B site of the perovskite causes some activity loss, even with respect to undoped LFM. As detailed by the XPS measurements discussed in section 3.1., the presence of B-site reducible cations at the catalyst surface plays a crucial catalytic role in the NO reduction reaction. Both A-site deficient perovskites exhibit the same reaction onset temperature, but $L_{0.85}FM$ is more active than $L_{0.7}FM$ over a wider range of temperatures. Therefore, it seems that the amount of defects has an optimum value for the peak activity and "over-doping" with vacancies leads to an activity decrease with increasing reaction temperature. Compared to the most active noble-metal containing Pd-impregnated LFM catalyst (termed "Pd0.02IM" in the following, corresponding to 0.02 wt.-% Pd impregnated on LFM) [2] (which already showed higher activity than the conventional Pd/Al_2O_3 catalyst for NO reduction by CO [2] and exhibited the lowest onset temperature and highest activity toward NO conversion over the entire temperature ranges), the onset temperatures for both La-deficient LFM perovskites are found at comparable temperatures (ca. 120 °C vs. 100 °C). The temperature-dependent catalytic profiles of the two A-site deficient catalytic profiles are more or less similar up to about 200 °C, whereas more differences arise between 200 °C and 320 °C. A similar trend is observed for the TOF as a function of reaction temperature. $La_{0.85}FM$ and $La_{0.7}FM$ feature the same reactivity trend at low reaction temperatures, but above around 170 °C, $La_{0.85}FM$ features consistently better than $La_{0.7}FM$. $L(FM)_{0.85}$ shows the worst catalytic behavior. Note that at around 300 °C, the activity of undoped LFM surpasses that of $L_{0.7}FM$ – again confirming the negative effect of overdoping with La deficient sites. Note that the TOF values cannot be directly compared to the Pd-containing catalyst, as different catalytically active sites prevail.

The product distribution profiles in Fig. 4 show that the formation of CO_2 is observed at first as the temperature increases, and with a slight delay, N_2O appears as a first product of the NO conversion with an intermediate maximum production rate. N_2 is the desired product of NO reactivity and always appears at higher temperatures. However, our results show that the presence of defects also has a great impact on product distribution. The formation of N_2O is limited in La-deficient perovskites, especially compared to LaPd0.02IM (cf. Fig. 4E). Considering the negative impact of N_2O, its suppression as a reactive intermediate greatly benefits these La-deficient catalysts from a technological viewpoint. We conclude that despite the high activity of

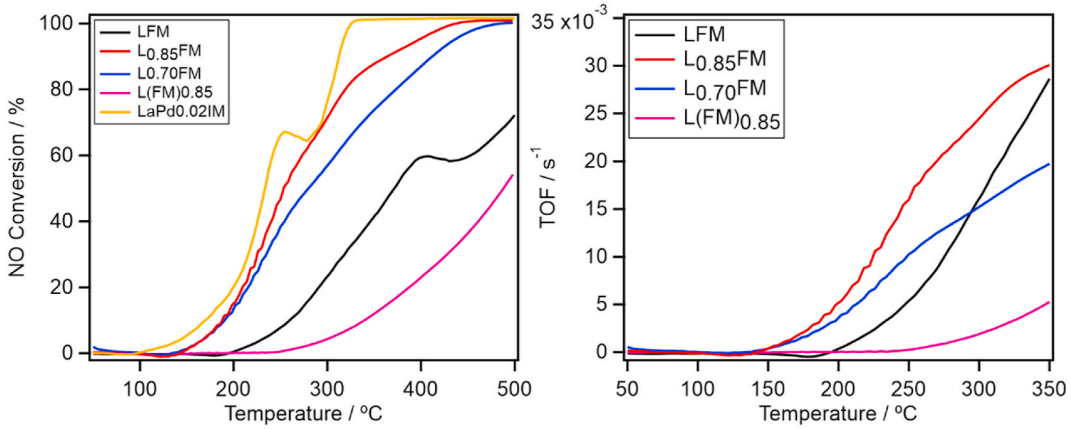

Fig. 3. Left panel: NO conversion profiles during NO reduction by CO under dry conditions for all LFM catalysts in comparison to the best-performing impregnated noble-metal-containing Pd-LFM catalyst. Right Panel: Calculated TOF values based on NO conversion following the procedure outlined in section 2.6. Total gas flow rate: 200 mL min^{-1} with a composition of (CO:NO:He = 1:1:98) of the inlet flow. Heating ramp: 2 °C min^{-1} between 50 °C and 500 °C. Sample mass: 200 mg.

the Pd-containing catalysts, they also produce high amounts of N_2O. In order to better compare and highlight how tuning the structure leads to the promotion of the noble metal-free catalysts to the same level or even exceeds the behavior of the corresponding noble metal-containing catalysts, the N_2 selectivity as a parameter is a more meaningful indicator. Therefore, the N_2 concentrations and N_2 selectivity are shown in Fig. S2 as a function of reaction temperature. The N_2 concentration profile of all catalysts except LFM and $L(FM)_{0.85}$ is comparable, but $L_{0.85}FM$ stands out in its performance with the highest N_2 concentrations between ca. 270 °C and 370 °C and consistently performs better than any other LFM catalyst.

To interpret the catalytic data in more detail, we provide below the representative set of literature-reported elementary reaction steps including reactant adsorption, reaction of intermediates and product desorption (Eqs. (1)–(12)). There is a general agreement regarding the contribution of a Langmuir-Hinshelwood type of NO + CO reaction mechanism. Within this mechanism, different mechanistic pathways are conceivable for the formation of various intermediates and final products, depending on the operating conditions. The elementary reaction steps highlighted in Eqs. (1)–(7) can occur both under dry and wet conditions and the water-gas shift reaction (Eqs. (8)–(12)) needs to be additionally considered in the presence of water. In each equation, S refers to step-specific catalytically active sites, but not all of them necessarily refer to the same site type and location. However, as it is shown in our catalytic test results under wet condition (Figs. S3 and S4), the formation of NH_3 is another product of NO reduction in the presence of water and its possible formation paths are discussed in detail in our previous works [2,26,28].

Moreover, our in-situ bulk and surface characterization during catalytic cycling under both dry and wet conditions indicates that the catalysts undergo both structural and chemical changes to oxygen deficient structures (see sections in situ XRD and in situ XPS). Therefore, in addition to purely Langmuir-Hinshelwood-type surface reaction steps related to adsorbed species from the gas phase, other, Mars-van Krevelen type reaction steps related to participation of reactive lattice oxygen need to be considered as well (Eqs. (1b)–(3b)). In order to check this claim in a more direct way we have performed additional CO-TPR experiments in the flow reactor setup under similar operating conditions to the NO + CO reaction condition with the difference that NO is excluded from the reaction feed. This set of experiments is designed to clarify the mechanistic behavior of the reaction network. In Fig. 5, the CO_2 formation profile during the CO-TPR reaction is shown in comparision with the formation of CO_2 and N_2O during the NO + CO reaction for $L_{0.85}FM$ and $L_{0.70}FM$. Here, we should point out that during CO-TPR, the source of oxygen to produce CO_2 is only lattice oxygen from the catalyst structure, but in the NO + CO reaction environment, an additional oxygen source stems from NO dissociation. These results clearly show that in the NO + CO reaction, in the temperatures range 50 °C–130 °C, and before formation of N_2O (which indicates beginning NO dissociation), CO_2 formation levels are almost comparable with the CO_2 levels during the CO-TPR reaction. This suggests, that the creation of oxygen vacancies near the surface regions is the first step for starting the NO + CO reaction. Interestingly, the effects of the presence of NO and occupying specific catalytic sites by its adsorption in the NO + CO reaction environment are only minor, as the level of CO_2 formation in the NO + CO reaction is only slightly lower than during the CO-TPR reaction. This is also in agreement with our previous result [2], that on these catalysts CO adsorbs more strongly than NO on the surface. Therefore, the contribution of lattice oxygen during CO oxidation (Eqs. (1b)–(3b)) and subsequent adsorption and (partial) dissociation of NO (and H_2O under wet condition) at reductively produced oxygen vacancies as an initial step for sequential reaction mechanism may significantly affect the overall catalyst performance. Scavenging of co-adsorbed oxygen by CO closes the reaction cycle, which would otherwise poison the surface for further adsorption and reaction. Therefore, according to this reaction mechanism we suggest here, the ease of CO oxidation by lattice oxygen leads to creation of oxygen vacancies and reduction of the steady state CO coverage on the catalyst. At the same time it enhances the dissociative adsorption of NO during catalytic operation. As will be shown in H_2-TPR and in-situ XRD section, creation of La-deficiency kinetically tunes the reducibility of the LFM catalysts. However, as it is clear from Fig. 5, although CO_2 production levels on $L_{0.70}FM$ are higher than for $L_{0.85}FM$ during CO-TPR - which means that $L_{0.7}FM$ has higher potential for reduction by CO - this trend is reversed during the NO + CO reaction. This observation, which will be also supported in the surface and bulk characterization experiments, clearly hints to the poisoning effects of lattice oxygen, whose continuously supply from the catalyst bulk as a result of overdoping with La-deficiency hinders NO adsorption and reaction (S denotes a surface adsorption site).

$$NO_{(g)} + S \rightarrow NO_{(ads)} \quad (1a)$$

$$CO_{(g)} + S \rightarrow CO_{(ads)} \quad (2a)$$

$$NO_{(ads)} + S \rightarrow N_{(ads)} + O_{(ads)} \quad (3)$$

$$2N_{(ads)} \rightarrow N_{2(g)} + 2S \quad (4)$$

$$CO_{(ads)} + O_{(ads)} \rightarrow CO_{2(g)} + 2S \quad (5)$$

$$NO_{(ads)} + N_{(ads)} \rightarrow N_2O_{(g)} + S \quad (6)$$

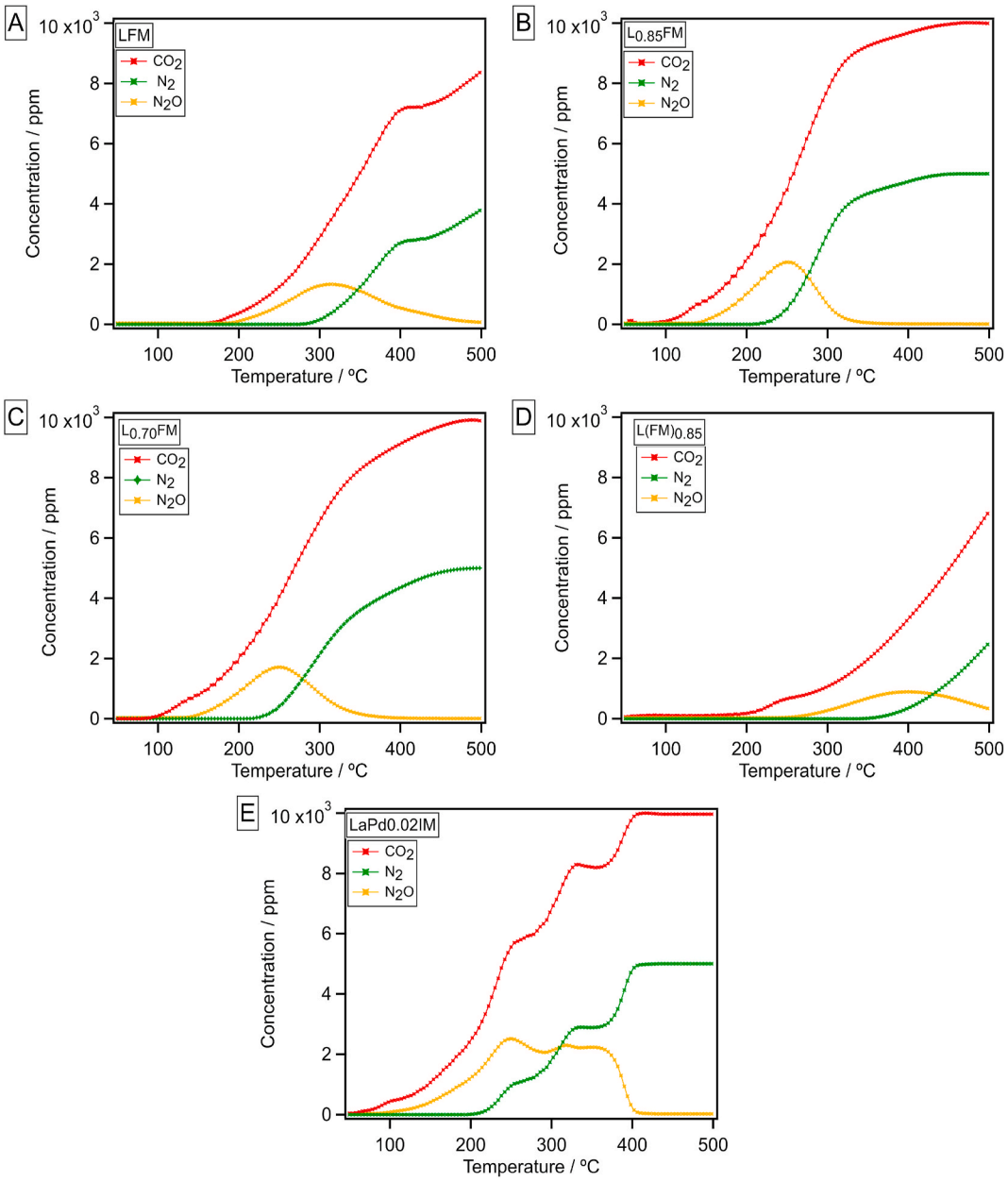

Fig. 4. Product distribution for all LFM samples in comparison to the impregnated noble-metal containing Pd-LFM catalyst during NO reduction by CO under dry conditions. Total gas flow rate: 200 mL min^{-1} with a composition of (CO:NO:He = 1:1:98) of the inlet flow. Heating ramp: 2 °C min^{-1} between 50 °C and 500 °C. Sample mass: 200 mg.

$$N_2O_{(ads)} + S \rightarrow N_{2(g)} + O_{(ads)} \quad (7)$$

$$H_2O_{(g)} + S \leftrightarrow H_2O_{(ads)} \quad (8)$$

$$H_2O_{(ads)} + S \leftrightarrow H_{(ads)} + OH_{(ads)} \quad (9)$$

$$CO_{(ads)} + OH_{(ads)} \rightarrow COOH_{(ads)} + S \quad (10)$$

$$COOH_{(ads)} \rightarrow CO_{2(g)} + H_{(ads)} \quad (11)$$

$$2H_{(ads)} \leftrightarrow H_{2(g)} + 2S \quad (12)$$

$$CO_{(ads)} + O_{lattice} \rightarrow CO_{2(g)} + V_O \quad (1b)$$

$$NO_{(ads)} + V_O \rightarrow N_{(ads)} + O_{(ads/lattice)} \quad (2b)$$

$$H_2O_{(g)} + O_{lattice} + V_O \rightarrow 2OH_{(ads)} \quad (3b)$$

According to the elementary reaction steps, mechanistic-wise, the formation of N_2O can be limited in two ways: 1) increasing the ability of the catalyst to dissociate NO, which causes an enhancement in the population of N species and a decrease in the population of molecularly adsorbed NO on the catalyst surface and 2) an intrinsic activity of catalyst to post-decomposition of pre-produced N_2O after re-adsorption on the catalyst surface [2]. Our results indicate that the second mechanism most likely prevents the formation of N_2O on La-deficient catalysts, displaying a higher selectivity toward N_2 than the Pd-containing catalyst. This follows from the fact, that as for the $L_{0.85}FM$ catalyst, although the NO conversion is not yet completed (e.g., at around 300 °C), the N_2O production rate is almost zero. In other words: if NO exists in the gas phase, enough molecularly adsorbed NO is found on the catalyst surface, leading to the formation of N_2O. Therefore, it is

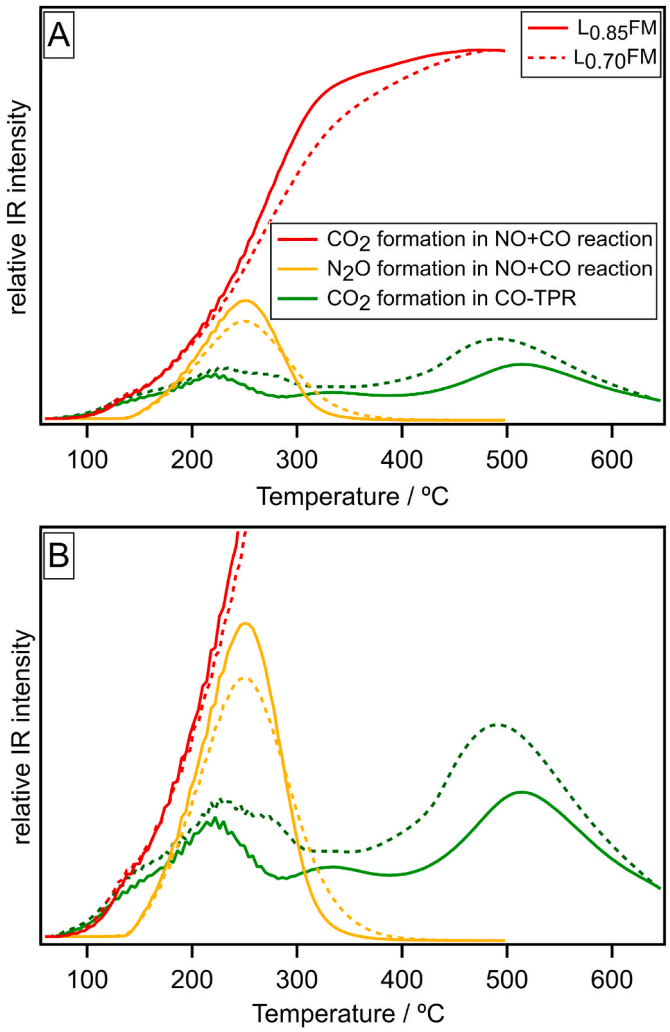

Fig. 5. Comparison of the formation of CO_2 during CO-TPR reaction with the formation of CO_2 and N_2O during the NO + CO reaction on $L_{0.85}$FM and $L_{0.70}$FM. CO-TPR: Total gas flow rate: 200 mL min^{-1} with a composition of (CO: He = 1:99) of the inlet flow. Heating ramp: 2 °C min^{-1} between 50 °C and 500 °C. Sample mass: 200 mg. NO + CO reaction: identical to Fig. 3.

reasonable to assume that N_2O is quickly consumed again immediately after production. In addition, according to additionally performed N_2O + CO reaction results (Fig. S5), the reaction onset temperature for N_2O reduction to N_2 on the LaPd0.02IM catalyst is almost similar to $L_{0.85}$FM and $L_{0.70}$FM catalysts. Compared to the NO conversion results (Fig. 3), where a clear difference in the reaction onset temperature between LaPd0.02IM and La-deficient catalysts is observed, it is clear that Pd is more active to reduce NO than N_2O. Of course, the observed higher activity of LaPd0.02IM in the N_2O + CO reaction at elevated temperatures compared to the La-deficient catalysts could be due to the creation of large amounts of oxygen vacancies that are active sites for N_2O decomposition. It is conceivable, that in the case of NO + CO reaction, these sites are occupied by NO instead of N_2O. Therefore, in the temperature range where NO conversion reaches 100 % on LaPd0.02IM catalyst, unreacted N_2O is also seen at the reactor outlet.

In order to interpret the qualitative course of the catalytic profile, we at first refer to the elementary reactions above and various reaction pathways, as discussed in detail in Ref. [2] and below. In brief, NO reduction by CO can in principle follow two main reaction branches, depending on NO and N_2O reactivity.

(1) $2NO + 2CO \rightarrow 2CO_2 + N_2$

(2) $2NO + CO \rightarrow N_2O + CO_2$; $N_2O + CO \rightarrow N_2 + CO_2$

The qualitative profile obtained for our lanthanum ferro manganite samples is typical for NO + CO reduction profiles found in literature for other ferrite, manganite or cobaltite perovskites [53–58]. As it also observed here, a gradual shift from route (2) with high N_2O production at low temperatures to route (1) at higher reaction temperatures is usually obtained. This naturally goes along with an intermediary N_2O peak. The appearance of a plateau-like feature in the NO conversion (sometimes even pronounced as a "peak") is a common phenomenon in the mechanistic transition from route (2) to route (1). As in our case this feature is observed both in the NO conversion and the N_2/CO_2 concentration, it appears to be connected to intermediate kinetic hindering of NO dissociation, which is overcome again at higher reaction temperatures. Corroborating literature reports, this feature is strongly dependent on catalyst composition [53–58]. This picture is consistent with additionally performed catalytic measurements in the N_2O + CO reaction (Fig. S5) and recent theoretical calculations on the NO + CO reaction over $LaMnO_3$ perovskites, revealing a bimolecular reaction mechanism involving a N_2O_2 reaction intermediate (from the reaction of two NO molecules) en route to N_2 and CO_2 [33].

In order to investigate the cycle and long-term stability of promotive defect structure in the NO + CO reaction environment, the activity of La deficient catalysts in a second catalytic cycle and upon performance at 100 h time-on-stream (for $L_{0.85}$FM) was tested (Figs. S6 and S7). $L_{0.85}$FM almost retains its activity during the second cycle. $L_{0.70}$FM becomes more active at temperatures higher than 250 °C, but remains inferior to the $L_{0.85}$FM catalyst. As will be shown in the XRD section (c.f. Fig. 8), the promotion of $L_{0.7}$FM during the second catalytic cycle can be related to the partial breakdown of the perovskite structure, the formation of the $MnFe_2O_4$ spinel phase, the exsolution of B site cations and the associated formation of a metal-perovskite phase boundary during the reaction. To eventually verify the hypothesis of activation by structural breakdown, we subjected $L_{0.70}$FM to a pre-treatment in hydrogen at 350 °C and tested $L_{0.70}$FM during two catalytic cycles (Fig. S6). In the H_2-reduced $L_{0.70}$FM sample, an increased number of oxygen vacancies and the presence of a metallic iron-perovskite phase boundary, are indeed the reason for activation during the first catalytic cycle. Partial sintering of the phase boundary and re-filling of H_2-induced oxygen vacancies during the first catalytic cycle could be a reason for activity loss of H_2-reduced $L_{0.70}$FM in the second catalytic cycle, as it is proven for Cu-perovskite phase boundaries in our previous work [26]. The catalytic data indicate that the exsolution is accelerated for $L_{0.70}$FM compared to $L_{0.85}$FM, as will be proven by H_2-TPR and in situ XRD/XPS in the subsequent sections. As shown in Fig. S7, the best-performing $L_{0.85}$FM catalyst retains its high NO conversion level during 100 h time-on-stream in the NO + CO reaction feed at 350 °C.

As water is an integral part of any technologically relevant deNO_x reaction mixture, we also tested the catalysts in the presence of 2.5 vol.-% water vapor ("wet conditions") (Fig. S3). The presence of water clearly diminishes the differences between LFM and all defect-promoted catalysts to some extent, and all catalysts are catalytically inferior to the Pd-containing catalyst. Water vapor has the ability to refill the oxygen vacancies and, therefore, adsorption of water on vacancies - which hinders their activity toward NO adsorption – is likely the reason for the lower activity of the catalysts in the presence of water. However, another important reason could be the consumption of CO (as a reductant) in the parallel occurring water gas shift reaction to form CO_2 and H_2. 100 % CO conversion, coupled with decreased NO reactivity (Fig. S4) and the parallel qualitatively detected H_2 formation, directly show the ability of the catalysts to act as catalysts in the water-gas shift equilibrium. The occurrence of NH_3 for all samples is also a strong hint towards water activation at oxygen vacancies. Focusing on the catalytically prospective LFM catalysts, we note that in contrast to under dry conditions, $L_{0.85}$FM performs not better than $L_{0.7}$FM. We, therefore, conclude that the activation mechanism of $L_{0.85}$FM discussed above –

related to in situ surface reduction during reaction - is essentially suppressed in the presence of water.

3.3. Assessing the redox properties of the materials with temperature-programmed H_2-reduction and O_2 - re-oxidation

As detailed in the elementary reactions section, one of the reaction mechanisms is related to the adsorption and dissociation of NO on reduced sites (i.e. oxygen vacancies), which leads to re-oxidation of those sites by replenishment with oxygen, we focus on determining the reducibility of the LFM catalysts to assess the reactivity of the catalysts in the NO reduction by CO.

To correlate the defect chemistry with the reduction propensity, Fig. 6 (left) shows the integral H_2 uptake of the catalysts as a function of temperature during the temperature-programmed reduction in hydrogen. A clear correlation of non-stoichiometry and reduction onset temperature, as well as quantitative final consumption of hydrogen, is evident. As observed for the deNO_x activity (Fig. 3), both catalysts with exclusive La deficiency exhibit similar onset temperatures at ~170 °C, which is ~60 °C lower than the starting temperature of LFM ($L_{0.7}$FM exclusively exhibits a small intermediate H_2 uptake peak, which is most likely associated with adsorption/desorption of a minute amount of physically adsorbed hydrogen). At ca. 300 °C, they become even more active, and accelerated H_2 uptake occurs. From 280 °C to 360 °C, $L_{0.85}$FM is more active than $L_{0.7}$FM and at 360 °C the uptake saturates, suggesting a diffusion-controlled reduction mechanism at temperatures higher than 360 °C. This saturation temperature is around 400 °C for $L_{0.7}$FM. The kinetic activation toward H_2 consumption of both La deficient perovskites compared to stoichiometric LFM could be due to the defective structure of these catalysts (most likely oxygen vacancies). Our results indicate an optimum amount of such oxygen vacancies for e.g. adsorption of NO or CO. Note that kinetic limitations still prevail for all catalysts at the highest uptake temperatures, as even in the isothermal sections hydrogen uptake is still observed. Hence, the oxygen vacancy concentration is representative for the chosen experimental conditions only and as such, naturally is a function of the chosen hydrogen treatment conditions. The most important result is that although $L_{0.7}$FM has a higher final capacity for hydrogen reduction/uptake than $L_{0.85}$FM ($18.6 \cdot 10^{-4}$ mol g^{-1} compared to $13.1 \cdot 10^{-4}$ mol g^{-1}, respectively), the latter exhibits a higher activity at intermediate temperatures. It is important to separate these two features: it indicates that as $L_{0.7}$FM has a higher number of defective structural sites, its propensity to reduction is higher, but its reduction progress is slower than for $L_{0.85}$FM in temperature ranges without strong diffusion limitation. Following a structural argument, as $L_{0.7}$FM exhibits smaller crystallite sizes and a higher surface area, it is expected to be more active than $L_{0.85}$FM in H_2-TPR. The same is known from the work of Gómez-Pérez et al. [11], who reported that clustering of La- and O-vacancy defects resulting from increasing x (for $x > 0.05$) in La-deficient $La_{2-x}CoTiO_{6-\delta}$ double perovskites causes a decrease in both ionic and electronic conductivity and we essentially prove that the same situation is prevalent for our samples.

To investigate the ability of defect titration using oxygen to quench oxygen vacancies produced during hydrogen reduction, temperature programmed oxidation in oxygen (O_2-TPO) was performed on $L_{0.70}$FM and $L_{0.85}$FM samples after H_2-TPR (Fig. 6, right). As for the integral O uptake as a function of temperature, both catalysts show similar onset temperatures, and the results are somewhat consistent with in-situ XRD results (Fig. 7 and S8-S10), where both catalysts show a similar trend in terms of onset temperature for structural reconstruction during re-oxidation steps. For both catalysts, we note that the O uptake is less than H_2 uptake, indicating that the quenching of all reduced sites/oxygen vacancies by O_2-titration is not possible. Higher oxidation temperatures and/or higher oxygen pressures are, therefore, necessary for full reversibility of the redox cycle. These data are important for interpreting reactivity profiles, where oxidation and reduction reactions occur simultaneously, and structural changes are likely to occur (section 3.4.).

3.4. Influence of defect chemistry on the bulk structural stability and dynamic exsolution of A- and B-site metal ions: reduction in hydrogen vs. re-oxidation in oxygen/water and stability in NO + CO/+H_2O reaction mixtures

To investigate the influence of defect chemistry on the stability and dynamic exsolution of B-site cations and the structural reconstruction of La deficient perovskites, in-situ X-ray diffraction measurements were conducted in various reaction environments:

- As the metal-perovskite interface potentially forming by decomposition of the perovskite has been shown to directly and beneficially influence the NO + CO reactivity [2,26,28], we at first tested the decomposition propensity in hydrogen in comparison to eventual direct decomposition in the NO + CO reaction mixture (Figs. 7 and 8)
- In order to investigate the ability to re-form the initial perovskite structures from the mixture of metallic and oxidic phases after the H_2-reduction process, the structural change of both La-deficient

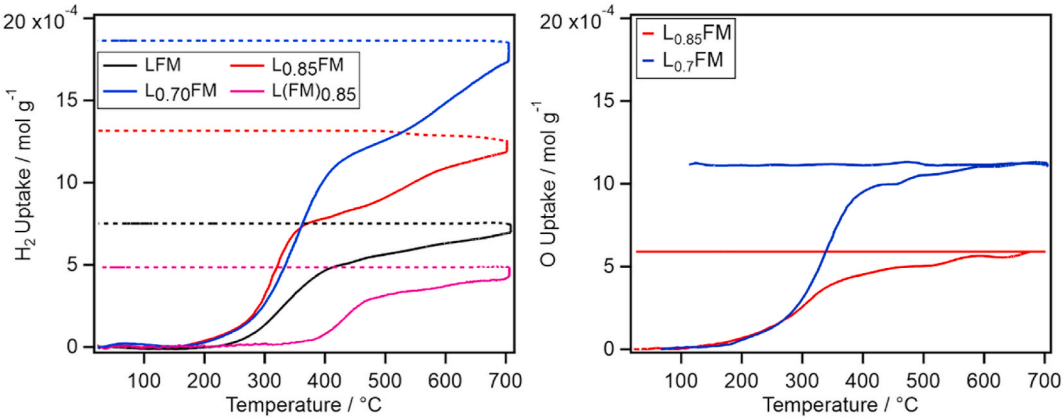

Fig. 6. Static temperature-programmed H_2-reduction (left) on LFM (black), $L_{0.85}$FM (red), $L_{0.7}$FM (blue), and $L(FM)_{0.85}$ (magenta) after pre-oxidation in flowing O_2 using an initial H_2 pressure of 125 mbar. Temperature program: heating from room temperature to 700 °C (10 °C min^{-1}/full lines), followed by an isothermal period at the maximum temperature (at 700 °C for 10 min/full line) and a cooling phase (10 °C min^{-1}/broken line). The integral H_2 uptake (black) is scaled on the left axis. Static temperature-programmed oxidation in oxygen on hydrogen pre-reduced samples is shown in the right Panel for $L_{0.85}$FM and $L_{0.7}$FM. The samples were heated initially at 125 mbar O_2 under the same conditions as the H_2-TPR. (For interpretation of the references to colour in this figure legend, the reader is referred to the Web version of this article.)

samples during re-oxidation in flowing oxygen has been monitored (Fig. S8).

- As water vapor is present as the main component in exhaust gas mixtures, and has significant effects on both catalyst structure and catalytic properties, the oxidation capability of water on H_2-pre-reduced perovskites, as well as its influence on the NO + CO reactivity, have been investigated (Figs. S9 and S10).

Fig. 7 shows the structural changes occurring during hydrogen reduction on $L_{0.70}$FM (left) and $L_{0.85}$FM (right). Segregation and the appearance of metallic iron (Fe^0) is the first step in structural changes for both catalysts, which is also associated with the chemical expansion of the perovskite structure. These results also indicate that Mn is more stable than Fe in these perovskite structures, in accordance with the literature [42,59]. As anticipated, $L_{0.85}$FM is more stable than $L_{0.70}$FM, and the formation of metallic Fe, therefore, starts at 375 °C on $L_{0.70}$FM, at slightly lower temperatures compared to $L_{0.85}$FM (390 °C). This indicates that a higher number of defects at the A site clearly renders the associated perovskite more structurally unstable. Final decomposition of the orthorhombic perovskite structure to MnO, Fe^0 and La_2O_3 starts at 640 °C for both catalysts and is completed after 20 min during the isothermal phase at 700 °C. During the cooling phase no structural changes happen and the final structure contains metallic Fe, MnO and La_2O_3.

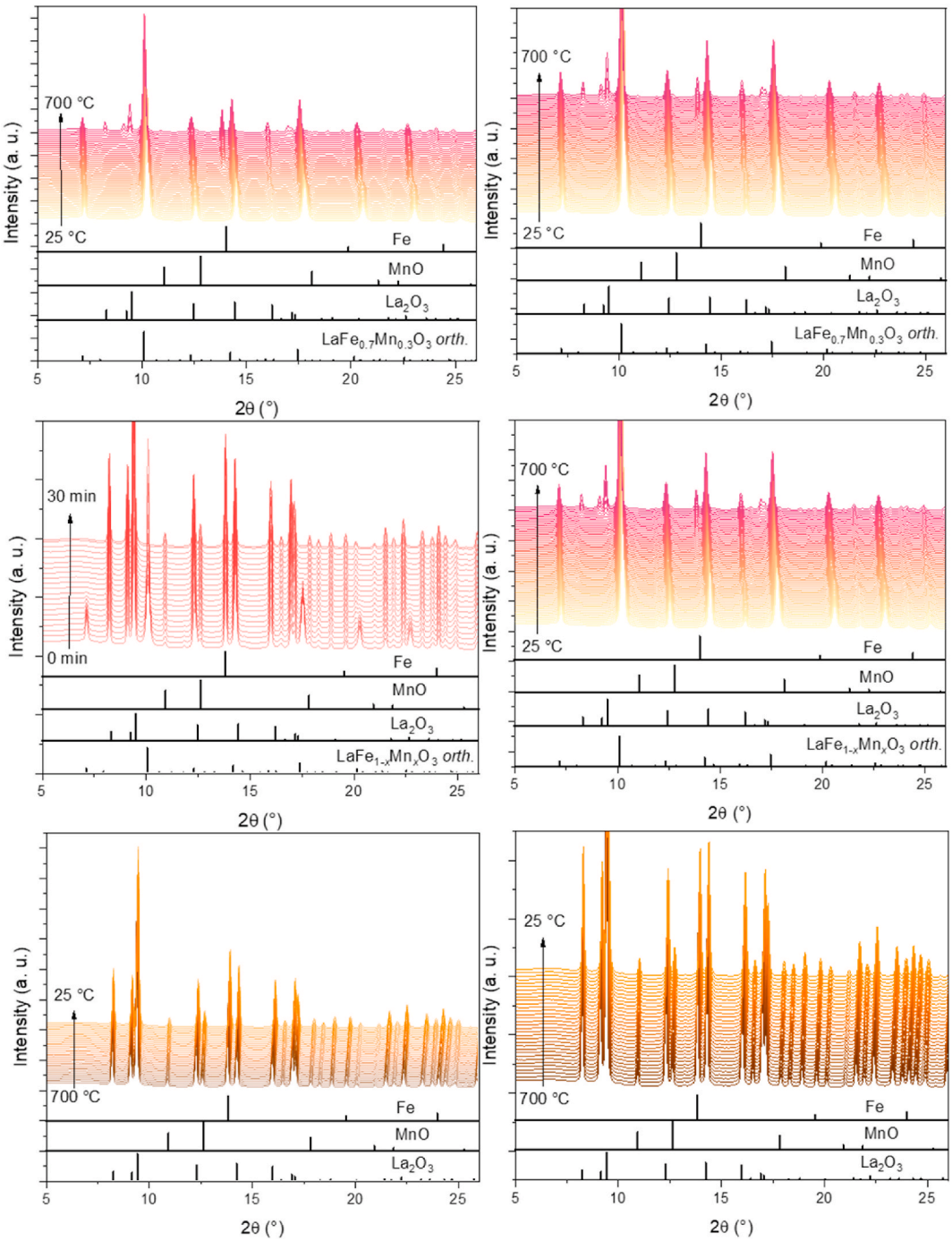

Fig. 7. In situ collected XRD patterns during reduction of $L_{0.70}$FM (left column) and $L_{0.85}$FM (right column) samples in flowing H_2 atmosphere from room temperature to 700 °C, followed by an isothermal phase at 700 °C for 30 min and re-cooling down to room temperature.

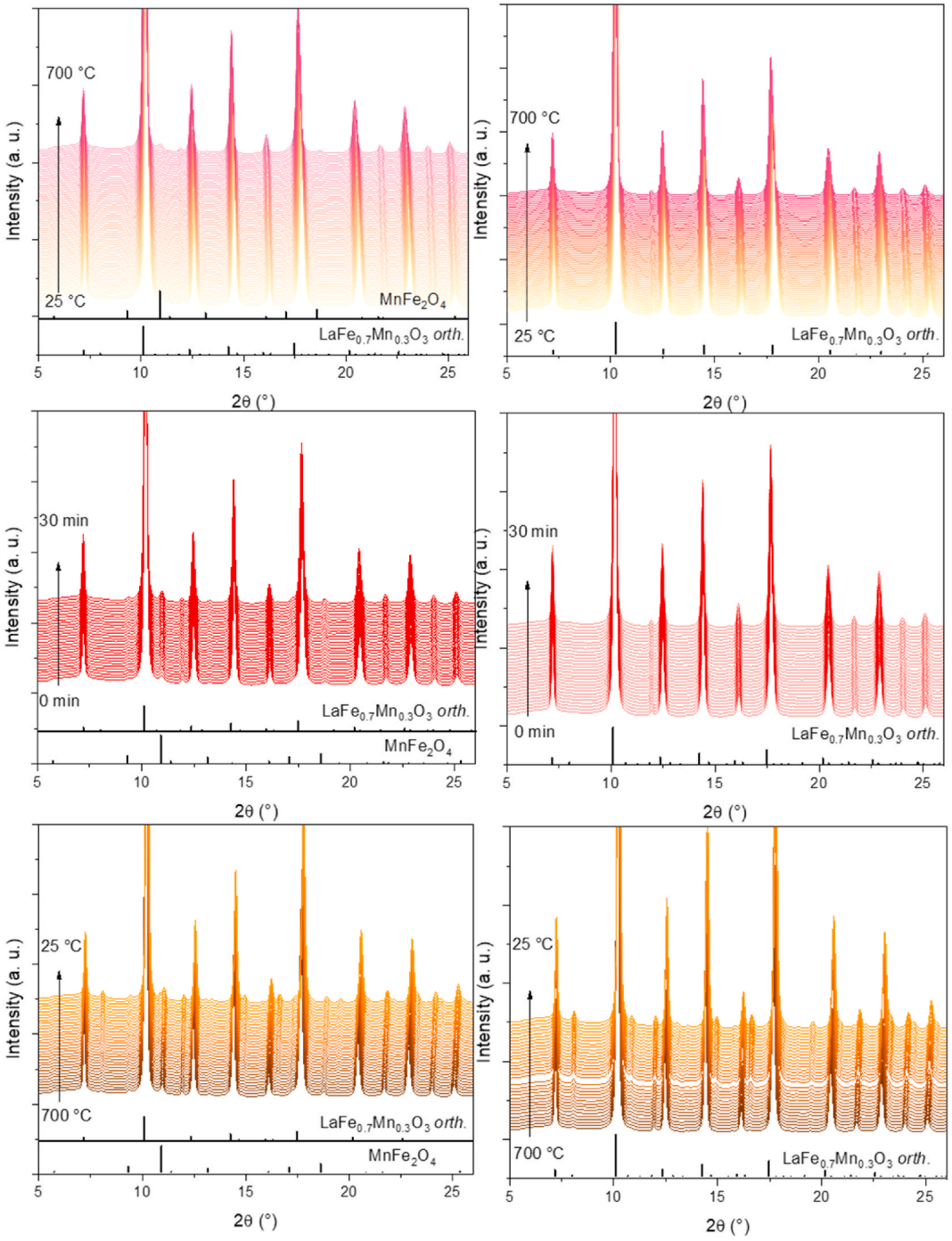

Fig. 8. In situ collected XRD patterns during heating of $L_{0.70}FM$ (left column) and $L_{0.85}FM$ (right column) samples in the NO + CO atmosphere from room temperature to 700 °C followed by an isothermal phase at 700 °C for 30 min and re-cooling to room temperature.

To test the possibility of perovskite re-formation (Fig. S8), previously exsolved Fe for both materials was oxidized during heating in O_2 and reacted with MnO at ~250 °C to form a $MnFe_2O_4$ spinel phase. At 450 °C, this phase decomposes, reacting with La_2O_3 to form a $LaFe_xMn_{1-x}O_3$ perovskite structure. During the isothermal step at 700 °C, the amounts of Fe_2O_3 and perovskite phases increase with time. Upon cooling, no significant structural changes occur, and the final samples contain an LFM perovskite with different Mn:Fe ratios, Fe_2O_3 and La_2O_3 oxides. We conclude that the structural changes during reduction are at least partially reversible under the chosen re-oxidation conditions.

If water vapor is used as a re-oxidation agent after hydrogen pre-reduction, for $L_{0.70}FM$ some of La_2O_3 is hydrolyzed to form $La(OH)_3$ at 70 °C, which is re-oxidized into c-La_2O_3 at 340 °C. Fe is subsequently oxidized and reacts with MnO at 250 °C to form the $MnFe_2O_4$ spinel phase. At 480 °C, an orthorhombic $La(FeMn)O_3$ perovskite starts to be formed from La_2O_3 and $MnFe_2O_4$. During the isothermal step at 700 °C, the transformation of La_2O_3 is nearly completed after 30 min, and after re-cooling, the final sample contains an LFM perovskite with a different Mn:Fe ratio from the starting material and the $MnFe_2O_4$ phase along with small amounts of La_2O_3. In the case of $L_{0.85}FM$, the sequence is somewhat similar, but the final structural mixture also contains Fe_2O_3 in addition to the perovskite and $MnFe_2O_4$ phases. The intermediate formation of $La(OH)_3$ has not been observed. Generally, these results show the ability of water vapor to re-oxidize reduced sites and refill oxygen

vacancies as active sites for NO absorption and dissociation. The only differences between water and oxygen as an oxidizing agent are the greater ability of the $MnFe_2O_4$ phase to withstand decomposition and the possibility of forming the $La(OH)_3$ phase in the presence of water.

An important aspect of a prospective $deNO_x$ catalyst is the structural stability under operational conditions or at least the understanding and steering of the structural changes in a beneficial way to improve the catalytic properties. We, therefore, subjected the A-site deficient perovskites to a realistic deNOx treatment with and without the presence of water. Fig. 8 shows the corresponding in situ collected X-ray diffractograms. $L_{0.70}FM$ partially decomposes into $MnFe_2O_4$ and an LFM perovskite with a different Mn:Fe ratio at 640 °C. During the isothermal step at 700 °C, the amount of $MnFe_2O_4$ is slightly increased, and during cooling, no prominent structural changes occur. The final sample contains LFM with different a Mn:Fe ratio from starting material and $MnFe_2O_4$. For $L_{0.85}FM$, the only structural change in the NO + CO reaction is a chemical expansion/contraction in the lattice after the experiments, again supporting the higher structural stability of $L_{0.85}FM$ compared to $L_{0.70}FM$ under $deNO_x$ conditions. The changes in the presence of water are essentially similar to those under dry conditions for both catalysts and are shown in Fig. S10. We have summarized the bulk structural transformations observed on the different LFM catalysts in selected treatments during in situ X-ray diffraction in Fig. 9.

Focusing on the fully oxidized LFM reference catalyst, Fig. S11 reveals that stoichiometric LFM is stable during H_2-TPR up to 700 °C and the only changes observed are a shift of XRD peaks to lower 2θ due to the creation of oxygen vacancies. Fig. S12 shows that reduction in the isothermal section causes a exsolution of small amounts of metallic Fe and formation of La_2O_3.

3.5. *Surface-chemical consequences of the presence of defects during the NO + CO reaction followed by in situ X-ray photoelectron spectroscopy*

As we have demonstrated the dependence of the structural instability on the A-site deficiency under reducing and $deNO_x$ conditions, the present section now focuses on the associated surface-chemical consequences of defect chemistry. We have restricted these experiments to the NO + CO reaction under dry conditions in the catalytically relevant temperature region up to 650 °C (Figs. 10 and 11). Fig. 10 shows the high-resolution spectra of C 1s and O 1s regions for the $L_{0.70}FM$ and $L_{0.85}FM$ catalysts during dry NO + CO reaction at seven isothermal temperature steps from 25 °C to 650 °C after normalizing their intensity to the La $3d_{5/2}$ area at the corresponding temperatures. Fig. 10 highlights the fitted Mn $2p_{3/2}$ region for both catalysts under the same experimental conditions (the fitted O 1s and Fe $2p_{3/2}$ regions are shown in the SI in Fig. S13). For experimental details of fitting, we refer to section 2.4. Since at temperatures higher than 350 °C, almost no adsorbed species can be seen in the C 1s region, these spectra are only shown up to 350 °C in Fig. 10. Although the amount of surface-bound carbon is very low (especially for $L_{0.70}$), the qualitative trend of a decreased total C 1s intensity at progressively higher reaction temperature is evident. These results clearly show that the intensity of carbonaceous species, which could result from the adsorption of CO and/or adventitious carbon, only decreases at temperatures higher than 150 °C, which is in good agreement with the onset temperature of NO reduction on these catalysts. Most importantly, it indicates that the reduction of NO starts when the inhibitory effects of adsorbed carbonaceous species on the surface decreases following desorption or oxidation using oxygen derived from catalyst surface during temperature increase. It is worth pointing out that NO adsorption on the catalyst surface and the presence of neighboring vacant sites for its dissociation are necessary for the start of the reaction. As mentioned in the catalytic section, the inhibitory effect of CO on adsorption and reduction of NO on LFM based catalysts is discussed in detail in our previous work [2].

As for the O 1 spectra, we shown them in Fig. 10 unfitted to make the overall intensity decrease at higher NO + CO reaction temperatures more clear (in correlation with the C 1s spectra), Fig. S13 in turn highlights the fitted components. According to the O 1s XP spectra of the $L_{0.85}FM$ catalyst, in addition to the changes in the peak shape during the progressing reaction (Fig. 10), the most important result is that the total intensity of O 1s region significantly decreases at temperatures higher than 550 °C. This affects the surface-bound oxygen containing components [2,7,60] at first (in agreement with the changes in the C 1s spectra) and at and above 450 °C also the lattice oxygen component [61–63], indicating partial reduction of the catalyst surface. The formation of oxygen vacancies is strongly supported by the changes in the Mn $2p_{3/2}$ peak (Fig. 11). Note, that in situ XRD at these temperatures did not indicate any bulk structural changes (Fig. 8), but the surface of $L_{0.85}FM$ already undergoes significant changes. These data are critical for interpreting the activity behavior of the catalysts. Of course, a minor

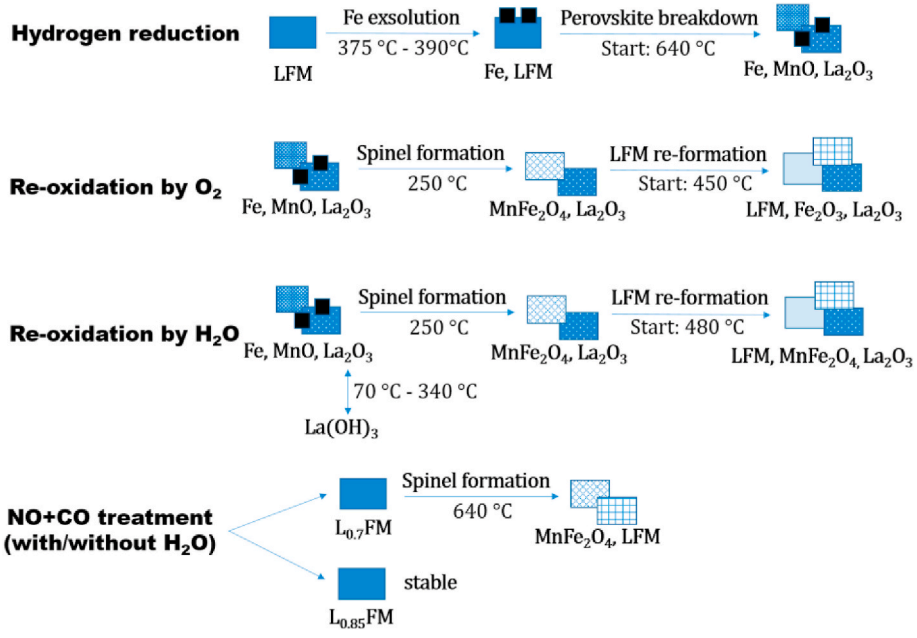

Fig. 9. Schematic representation of the bulk structural transformations observed on the different LFM catalysts in selected treatments during in situ X-ray diffraction.

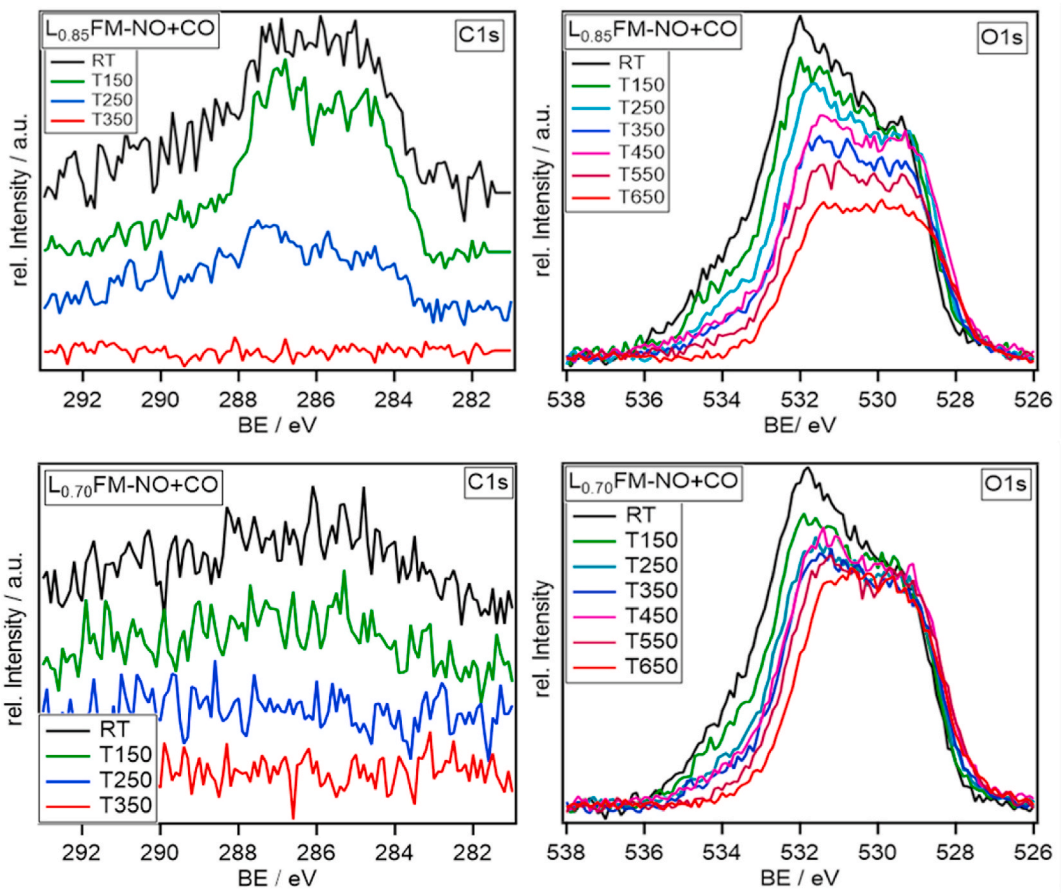

Fig. 10. C 1s and O 1s XP spectra recorded in situ under CO + NO atmosphere at temperatures between 25 °C and 650 °C for $L_{0.85}FM$ and $L_{0.70}FM$. The intensity of all spectra is normalized to the La $3d_{5/2}$ area at the corresponding temperatures.

temperature-delayed effect due to the decreased experimental pressure regime in NAP-XP spectroscopy, compared to in situ XRD or flow reactor conditions, cannot be excluded. $L_{0.70}FM$ shows the same trend in intensity decrease with two important differences: the overall intensity decrease is not as prominent and the lattice oxygen component features no change at all. We relate this to a continuous oxygen supply from the catalyst bulk to the surface because of a high concentration of La deficient sites, corroborating the H_2-TPR and CO-TPR results. This observation is the key point for interpreting the lower deNO_x activity of $L_{0.70}FM$ compared to $L_{0.85}FM$: the oxygen-deficient surface structure is expected to be more active for NO reduction.

The Fe $2p_{3/2}$ XP spectra (Fig. S13) have been tentatively fitted with three peaks at 715.0 eV, 712.0 eV and 709.4 eV denoted as a-c in agreement with literature. Peak (a) is related to Fe^{4+} [60,64] and possibly also with Fe^{3+} in tetrahedral coordination [65], while peaks b and c are associated with Fe^{3+} and Fe^{2+} [66,67], respectively. According to the results, it is clear that the main component of Fe species in both catalysts is Fe^{3+} in the whole temperature range, and Fe^{2+} only appears at temperatures higher than 350 °C, which is accompanied by a decrease in the Fe^{3+} intensity. In general, the Fe $2p_{3/2}$ region features the expected changes.

For the Mn $2p_{3/2}$ region (Fig. 11), which shows the most prominent changes upon the NO + CO reaction, four peaks have been used for fitting and are denoted as a-d from highest binding energy to lowest. The presence/absence of a distinct Mn^{2+} satellite typically found at 647.0 eV (peak a) is useful to detect Mn^{2+} components, which exhibit their main peak at 640.3 eV (peak d) [7,68]. Peaks b and c at binding energies of 644.0 eV and 641.5 eV can be assigned to Mn^{4+} and Mn^{3+} components, respectively [68,69]. Most of the Mn species are present as Mn^{4+} in both perovskites and by progressing reaction, these components are converted to Mn^{3+}. At higher temperatures (around 550 °C) Mn^{2+} is also visible in the spectra in consistence with the formation of the $MnFe_2O_4$ spinel phase (Fig. 8), where Mn is mostly present in the valence state (II) [68–70].

The evolution of the O 1s peak is also shown in Fig. S13 in more detail compared to Fig. 10. We have tentatively fitted this peak with three components at 534.5 eV, 531.7 eV and 529.4 eV marked as a, b and c, respectively. The lowest binding energy peak is assigned to lattice O species [62,71,72]. The second peak b is assigned to oxygen-containing surface species, and in particular, the third peak a at highest binding energies is attributed to adsorbed water [2,7,60]. At room temperature and under NO + CO gas atmosphere, the contribution of surface-adsorbed oxygenate components is dominant for both perovskites. The main aspect is that by increasing temperature, the component of the spectrum at higher binding energies (adsorbed O-species and water) decreases and at the same time, the contribution of lattice oxygen increases.

Considering all in situ XP results in combination with the in situ XRD results (Fig. 8), it can be concluded that NO + CO reaction is a net reducing environment for both catalysts with the difference that the reduction in $L_{0.85}FM$ catalyst is limited to only near-surface regions. As it is safe from the effects of "surface poisoning" with bulk oxygen and it retains a stable structure, it is a promising candidate for deNO_x applications from a technical point of view.

4. Conclusions

By adjusting the defect level during the synthesis of a number of A- and B-site deficient perovskites, we highlight that non-stoichiometry can increase the catalytic activity and selectivity to N_2 in the selective

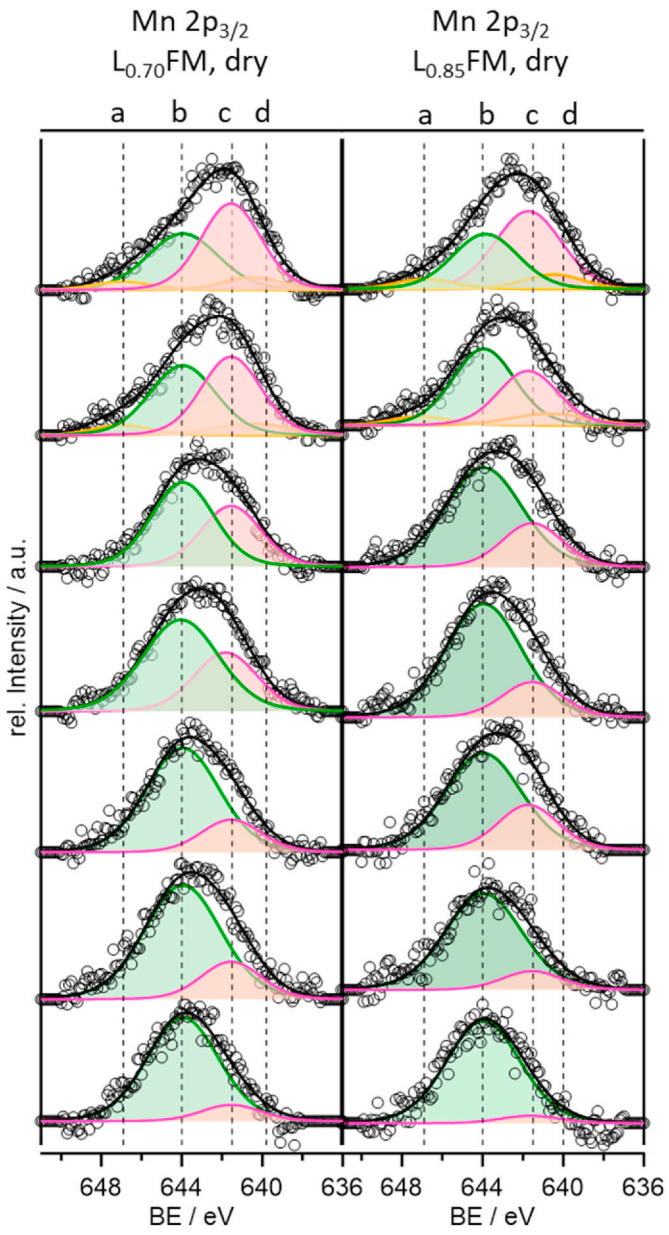

Fig. 11. Deconvoluted Mn $2p_{3/2}$ XP spectra recorded in situ under CO + NO atmosphere at seven temperatures between 25 °C and 650 °C for $L_{0.70}FM$ and $L_{0.85}FM$.

catalytic reduction of NO by CO on noble metal-free LFM-based perovskites. A prerequisite is La deficiency. Optimal steering of the redox chemistry to reduce the near-surface regions in the NO + CO reaction atmospheres at low temperatures is hereby the key factor. Surface enrichment by reducible B site cations and a proper design of structural defects result from the optimum introduction of La defects leading to in-situ reduction of only surface-near regions by CO oxidation and subsequently providing oxygen vacancies for adsorption (or re-adsorption) and the reaction of NO and intermediate N_2O. Over-doping with La - associated defects leads to structural instability of the perovskites and also a continuous supply of oxygen from the bulk structure to the catalyst surface at elevated temperatures, that leads to surface poisoning by oxygen. Introduction of vacancies at the B site leads to surface enrichment by non-reducible La cations, which leads to a suppressed catalyst activity to values even lower than the stoichiometric LFM reference catalyst. One particular outcome of the work is the development of a completely noble-meal free perovskite catalyst with improved catalytic properties. Correlated to a Pd-containing perovskite material, the optimized LFM catalyst designed in the present work exhibits comparable NO conversion rates with improved N_2 selectivity at intermediate temperatures between 250 °C and 350 °C and accelerated N_2O decomposition kinetics. La deficiency, therefore, can compensate the absence of the noble metal and its beneficial catalytic properties.

CRediT authorship contribution statement

Asghar Mohammadi: Funding acquisition, Investigation. **Christoph W. Thurner:** Data curation, Formal analysis, Investigation. **Leander Haug:** Data curation, Formal analysis, Investigation. **Maged F. Bekheet:** Data curation, Formal analysis, Investigation. **Julian T. Müller:** Data curation, Formal analysis, Investigation. **Aleksander Gurlo:** Writing - review & editing. **Clivia Hejny:** Data curation, Formal analysis, Investigation. **Parastoo Delir Kheyrollahi Nezhad:** Data curation, Formal analysis, Investigation. **Daniel Winkler:** Data curation, Formal analysis, Investigation. **Wiebke Riedel:** Data curation, Formal analysis, Investigation. **Simon Penner:** Conceptualization, Funding acquisition, Supervision, Writing - original draft.

Declaration of competing interest

The authors declare that they have no known competing financial interests or personal relationships that could have appeared to influence the work reported in this paper.

Data availability

Data will be made available on request.

Acknowledgments

A. Mohammadi thanks the FWF (Austrian Science foundation) for financial support under the project P 35770 –N. The work has been performed within the framework of the research platform “Advanced Materials” at UI. We would like to thank Harald Link for collecting ICP-OES Data. The authors thank the Advanced Light Source, which is supported by the Director, Office of Science, Office of Basic Energy Sciences, of the U.S. Department of Energy under Contract No. DE-AC02-05CH11231, and where the in situ XRD measurements were conducted at beamline 12.2.2 in the framework of the AP proposals (ALS-08408 and ALS-11921).

Appendix A. Supplementary data

Supplementary data to this article can be found online at https://doi.org/10.1016/j.mtchem.2024.101910.

References

[1] C.K. Lambert, Current state of the art and future needs for automotive exhaust catalysis, Nat. Catal. 2 (2019) 554–557.
[2] A. Mohammadi, A. Farzi, C. Thurner, B. Klötzer, S. Schwarz, J. Bernardi, A. Niaei, S. Penner, Tailoring the metal-perovskite interface for promotional steering of the catalytic NO reduction by CO in the presence of H_2O on Pd-lanthanum iron manganite composites, Appl. Catal., B 307 (2022) 121160.
[3] S. Rood, S. Eslava, A. Manigrasso, C. Bannister, Recent advances in gasoline three-way catalyst formulation: a review, Proc. Inst. Mech. Eng., Part D 234 (2020) 936–949.
[4] K. Skalska, J.S. Miller, S. Ledakowicz, Trends in NO_x abatement: a review, Sci. Total Environ. 408 (2010) 3976–3989.
[5] R. Di Monte, J. Kaspar, P. Fornasiero, M. Graziani, C. Paze, G. Gubitosa, NO reduction by CO over $Pd/Ce_{0.6}Zr_{0.4}O_2$-Al_2O_3 catalysts: in situ FT-IR studies of NO and CO adsorption, Inorg. Chim. Acta. 334 (2002) 318–326.
[6] R.J. Farrauto, M. Deeba, S. Alerasool, Gasoline automobile catalysis and its historical journey to cleaner air, Nat. Catal. 2 (2019) 603–613.
[7] M. Grünbacher, A. Tarjomannejad, P.D.K. Nezhad, C. Praty, K. Ploner, A. Mohammadi, A. Niaei, B. Klötzer, S. Schwarz, J. Bernardi, Promotion of La

$(Cu_{0.7}Mn_{0.3})_{0.98}M_{0.02}O_{3-\delta}$ (M= Pd, Pt, Ru and Rh) perovskite catalysts by noble metals for the reduction of NO by CO, J. Catal. 379 (2019) 18–32.
[8] K. Ueda, M. Tsuji, J. Ohyama, A. Satsuma, Active coordination sites of Co spinel oxides for NO reduction by CO, Catal, Today Off. 411 (2023) 113816.
[9] A. Garbujo, M. Pacella, M. Natile, M. Guiotto, J. Fabro, P. Canu, A. Glisenti, On A-doping strategy for tuning the TWC catalytic performance of perovskite based catalysts, Appl. Catal., A 544 (2017) 94–107.
[10] A. Gómez-Pérez, M.T. Azcondo, M. Yuste, J.C. Pérez-Flores, N. Bonanos, F. Porcher, A. Muñoz-Noval, M. Hoelzel, F. García-Alvarado, U. Amador, The A-cation deficient perovskite series $La_{2-x}CoTiO_{6-\delta}$ ($0 \leq x \leq 0.20$): new components for potential SOFC composite cathodes, J. Mater. Chem. A 4 (2016) 3386–3397.
[11] J.C. Pérez-Flores, D. Perez-Coll, S. Garcia-Martin, C. Ritter, G.C. Mather, J. Canales-Vazquez, M. Galvez-Sanchez, F. Garcia-Alvarado, U. Amador, A-And B-site ordering in the A-cation-deficient perovskite series $La_{2-x}NiTiO_{6-\delta}$ ($0 \leq x < 0.20$) and evaluation as potential cathodes for solid oxide fuel cells, Chem. Mater. 25 (2013) 2484–2494.
[12] J. Wu, Y. Zheng, J.-P. Dacquin, N. Djelal, C. Cordier, C. Dujardin, P. Granger, Impact of dual calcium and manganese substitution of La-deficient perovskites on structural and related catalytic properties: future opportunities in next three-way-catalyst generation? Appl. Catal., A 619 (2021) 118137.
[13] H. Arandiyan, S.S. Mofarah, C.C. Sorrell, E. Doustkhah, B. Sajjadi, D. Hao, Y. Wang, H. Sun, B.J. Ni, M. Rezaei, Defect engineering of oxide perovskites for catalysis and energy storage: synthesis of chemistry and materials science, Chem. Soc. Rev. 50 (2021) 10116–10211.
[14] D. Mutter, D.F. Urban, C. Elsässer, R. Schierholz, S.A. Heuer, T. Ohlerth, H. Kungl, R.-A. Eichel, Defects and phase formation in non-stoichiometric $LaFeO_3$: a combined theoretical and experimental study, Chem. Mater. 33 (2021) 9473–9485.
[15] S. Yakovlev, V. Kharton, A. Yaremchenko, A. Kovalevsky, E. Naumovich, J. Frade, Mixed conductivity, thermal expansion and defect chemistry of A-site deficient $LaNi_{0.5}Ti_{0.5}O_{3-\delta}$, J. Eur. Ceram. Soc. 27 (2007) 4279–4282.
[16] J. Chen, M. Shen, X. Wang, G. Qi, J. Wang, W. Li, The influence of nonstoichiometry on $LaMnO_3$ perovskite for catalytic NO oxidation, Appl. Catal., B 134 (2013) 251–257.
[17] R. Spinicci, A. Delmastro, S. Ronchetti, A. Tofanari, Catalytic behaviour of stoichiometric and non-stoichiometric $LaMnO_3$ perovskite towards methane combustion, Mater. Chem. Phys. 78 (2003) 393–399.
[18] Z. Wang, Q. Xu, J. Sun, J. Pan, H. Zhang, Room temperature magnetocaloric effect of La-deficient bulk perovskite manganite $La_{0.7}MnO_{3-\delta}$, Phys. B: Condens. 406 (2011) 1436–1440.
[19] H. Vincent, M. Audier, S. Pignard, G. Dezanneau, J. Senateur, Crystal structure transformations of a magnetoresistive $La_{0.8}MnO_{3-\delta}$ thin film, J. Solid State Chem. 164 (2002) 177–187.
[20] J. Alonso, M. Martinez-Lope, M. Casais, J. MacManus-Driscoll, P.S. de Silva, L. Cohen, M. Fernandez-Diaz, Non-stoichiometry, structural defects and properties of $LaMnO_{3+\delta}$ with high δ values ($0.11 \leq \delta \leq 0.29$), J. Mater. Chem. 7 (1997) 2139–2144.
[21] M. Wołcyrz, R. Horyń, F. Bourée, E. Bukowska, Structural defects in $LaMnO_3$ phase studied by neutron diffraction, J. Alloys Compd. 353 (2003) 170–174.
[22] A. Leontiou, A. Ladavos, P. Pomonis, Catalytic NO reduction with CO on $La_{1-x}Sr_x(Fe^{3+}/Fe^{4+})O_{3\pm\delta}$ perovskite-type mixed oxides (x= 0.00, 0.15, 0.30, 0.40, 0.60, 0.70, 0.80, and 0.90), Appl. Catal., A 241 (2003) 133–141.
[23] A. Giannakas, A. Ladavos, P. Pomonis, Preparation, characterization and investigation of catalytic activity for NO + CO reaction of $LaMnO_3$ and $LaFeO_3$ perovskites prepared via microemulsion method, Appl. Catal., B 49 (2004) 147–158.
[24] V.C. Belessi, C.N. Costa, T.V. Bakas, T. Anastasiadou, P.J. Pomonis, A. M. Efstathiou, Catalytic behavior of La–Sr–Ce–Fe–O mixed oxidic/perovskitic systems for the NO + CO and NO+ CH_4+ O_2 (lean-NO_x) reactions, Catal. Today 59 (2000) 347–363.
[25] S. Peter, E. Garbowski, V. Perrichon, M. Primet, NO reduction by CO over aluminate-supported perovskites, Catal. Lett. 70 (2000) 27–33.
[26] C.W. Thurner, N. Bonmassar, D. Winkler, L. Haug, K. Ploner, P. Delir Kheyrollahi Nezhad, X. Drexler, A. Mohammadi, P.A. van Aken, J. Kunze-Liebhäuser, Who does the job? How copper can replace noble metals in sustainable catalysis by the formation of copper–mixed oxide interfaces, ACS Catal. 12 (2022) 7696–7708.
[27] A. Glisenti, M. Pacella, M. Guiotto, M. Natile, P. Canu, Largely Cu-doped $LaCo_{1-x}Cu_xO_3$ perovskites for TWC: toward new PGM-free catalysts, Appl. Catal., B 180 (2016) 94–105.
[28] C.W. Thurner, X. Drexler, L. Haug, D. Winkler, J. Kunze-Liebhäuser, J. Bernardi, B. Klötzer, S. Penner, When copper is not enough: advantages and drawbacks of using copper in de-NO_x reactions over lanthanum manganite perovskite structures, Appl. Catal., B 331 (2023) 122693.
[29] H. Tanaka, N. Mizuno, M. Misono, Catalytic activity and structural stability of La0.9Ce0.1Co1−xFexO3 perovskite catalysts for automotive emissions control, Appl. Catal., A 244 (371-382), doi: 10.1016/S0926-860X(02)00609-9.
[30] M. Daturi, N. Bion, J. Saussey, J.-C. Lavalley, C. Hedouin, T. Seguelong, G. Blanchard, Evidence of a lacunar mechanism for deNO_x activity in ceria-based catalysts, Phys. Chem. Chem. Phys. 3 (2001) 252–255.
[31] K. Kakaei, M.D. Esrafili, A. Ehsani, Gas convertor and storage, Interface Sci. Technol. 27 (2019) 387–437. Elsevier.
[32] C.-M. Cho, N. Nunotani, N. Imanaka, Effect of oxygen vacancies on direct N_2O decomposition over ZrO_2-Y_2O_3 catalysts, J. Asian Ceram. Soc. 7 (2019) 518–523.
[33] X. Yu, J. Liu, Y. Yang, Z. Wang, Y. Zheng, A catalytic reaction scheme for NO reduction by CO over Mn-terminated LaMnO3 perovskite: a DFT study Fuel Processing, Technol. 216 (2021) 106798, 10.1016{j.fuproc.2021.106798.
[34] A. Doran, L. Schlicker, C. Beavers, S. Bhat, M. Bekheet, A. Gurlo, Compact low power infrared tube furnace for in situ X-ray powder diffraction, Rev. Sci. Instrum. 88 (2017) 013903.
[35] L. Schlicker, A. Doran, P. Schneppmüller, A. Gili, M. Czasny, S. Penner, A. Gurlo, Transmission in situ and operando high temperature X-ray powder diffraction in variable gaseous environments, Rev. Sci. Instrum. 89 (2018) 033904.
[36] J. Rodriguez-Carvajal, Recent developments of the program FULLPROF, Comm. Powder Diffr. (CPD) Newsl. 26 (2001) 12–19.
[37] J. Kim, Y. Kim, M. Feree, S. Gunduz, A.C. co, M. Kim, U. Ozkan, In-situ exsolution of bimetallic CoFe nanoparticles on (La,Sr)FeO3 perovskite: its effect on electrocatalytic oxidative coupling of methane, Appl. Catal., B 321 (2023) 122026, https://doi.org/10.1016/j.apcatb.2022.122026.
[38] R. Sun, L. Shen, S. Wang, H. Bai, CO conversion over LaFeO3 perovskite during chemical looping processes: influences of Ca-doping and oxygen species, Appl. Catal., B 316 (2022) 121598, https://doi.org/10.1016/j.apcatb.2022.121598.
[39] R. Mandal, Y. Mahton, C. Sowjanya, K. Sanket, S. Behera, S. Pratihar, Electrocatalytic behaviour of Cu-substituted La0.5Sr0.5Co0.8Fe0.2-xCuxO3-δ (x = 0–0.2) perovskite oxides, J. Solid State Chem. 317 (2023) 123668.
[40] M. Abrishami, M. Mohammadi, M. Sotoudeh, Photocatalytic dye decomposition over CaMnO3−δ and Pr0.5Ca0.5MnO3: a combined XPS and DFT study, Catalysts 12 (2022) 1728, https://doi.org/10.3390/cryst12121728.
[41] G. Mekhemer, H. Mohamad, A. Bumajad, M. Zaki, Lattice-charge imbalance and redox catalysis over perovskite-type ferrite- and manganite-based mixed oxides as studied by XRD, FTIR, UV–Vis DRS, and XPS, Sci. Rep. 13 (2023) 7453, https://doi.org/10.1038/s41598-023-34065-3.
[42] P.I. Cowin, R. Lan, C.T. Petit, D. Du, K. Xie, H. Wang, S. Tao, Conductivity and redox stability of new perovskite oxides $SrFe_{0.7}TM_{0.2}Ti_{0.1}O_{3-\delta}$ (TM= Mn, Fe, Co, Ni, Cu), Solid State Ionics 301 (2017) 99–105.
[43] R. Bliem, D. Kim, J. Wang, E.J. Crumlin, B. Yildiz, Hf deposition stabilizes the surface chemistry of perovskite manganite oxide, J. Phys. Chem. C 125 (2021) 3346–3354.
[44] B. Koo, K. Kim, J.K. Kim, H. Kwon, J.W. Han, W. Jung, Sr segregation in perovskite oxides: why it happens and how it exists, Joule 2 (2018) 1476–1499.
[45] Y.N. Lee, R.M. Lago, J.L.G. Fierro, V. Cortes, F. Sapina, E. Martinez, Surface properties and catalytic performance for ethane combustion of $La_{1-x}K_xMnO_{3+\delta}$ perovskites, Appl. Catal., A 207 (2001) 17–24.
[46] J. Wu, J.-P. Dacquin, C. Cordier, C. Dujardin, P. Granger, Optimization of the composition of perovskite type materials for further elaboration of four-way catalysts for gasoline engine, Top. Catal. 62 (2019) 368–375.
[47] Y. Wu, X. Ni, A. Beaurain, C. Dujardin, P. Granger, Stoichiometric and non-stoichiometric perovskite-based catalysts: consequences on surface properties and on catalytic performances in the decomposition of N_2O from nitric acid plants, Appl. Catal., B 125 (2012) 149–157.
[48] B.P. Barbero, L.E. Cadús, S.G. Marchetti, Determination of Fe(IV) species in partially substituted perovskite $La_{0.6}Ca_{0.4}FeO_3$, Hyperfine Interact. 194 (2009) 367.
[49] A.A. Ansari, S.F. Adil, M. Alam, N. Ahmad, M.E. Assal, J.P. Labis, A. Alwarthan, Catalytic performance of the Ce-doped $LaCoO_3$ perovskite nanoparticles, Sci. Rep. 10 (2020) 15012.
[50] O. Yamamoto, Y. Takeda, R. Kanno, M. Noda, Perovskite-type oxides as oxygen electrodes for high temperature oxide fuel cells, Solid State Ionics 22 (1987) 241–246.
[51] S. Carter, A. Selcuk, R. Chater, J. Kajda, J. Kilner, a.B. Steele, Oxygen transport in selected nonstoichiometric perovskite-structure oxides, Solid State Ionics 53 (1992) 597–605.
[52] T. Götsch, N. Köpfle, M. Grünbacher, J. Bernardi, E.A. Carbonio, M. Hävecker, A. Knop-Gericke, M.F. Bekheet, L. Schlicker, A. Doran, Crystallographic and electronic evolution of lanthanum strontium ferrite ($La_{0.6}Sr_{0.4}FeO_{3-\delta}$) thin film and bulk model systems during iron exsolution, Phys. Chem. Chem. Phys. 21 (2019) 3781–3794.
[53] R. Zhang, A. Villanueva, H. Alamdari, S. Kaliaguine, Reduction of NO by CO over nanoscale LaCo1−xCuxO3 and LaMn1−xCuxO3 perovskites, J. Mol. Catal. 258 (2006) 22–34, https://doi.org/10.1016/j.molcata.2006.05.008.
[54] S.D. Peter, E. Garbowski, V. Perrichon, M. Primet, NO reduction by CO over aluminate-supported perovskites, Catal. Lett. 70 (2000) 27–33, https://doi.org/10.1023/A:1019027619209.
[55] Y. Wu, et al., NO reduction by CO over highly active and stable perovskite oxide catalysts La0.8Ce0.2M0.25Co0.75O3 (M = Cu, Mn, Fe): effect of the role in B site, Ind. Eng. Chem. Res. 57 (2018) 15670–15682.
[56] R.K. C de Lima, M.S. Batista, M. Wallau, E.A. Sanches, Y.P. Mascarenhas, E. A. Urqieta-Gonzalez, High specific surface area LaFeCo perovskites—synthesis by nanocasting and catalytic behavior in the reduction of NO with CO, Appl. Catal., B 90 (2009) 441–450.
[57] J. Hwang, et al., Regulating oxygen activity of perovskites to promote NOx oxidation and reduction kinetics, Nat. Catal. 4 (2021) 663–673, https://doi.org/10.1038/s41929-021-00656-4.
[58] R. Zhang, H. Alamdari, S. Kaliaguine, Fe-based perovskites substituted by copper and palladium for NO + CO reaction, J. Catal. 242 (2006) 241–253, https://doi.org/10.1016/j.jcat.2006.05.033.
[59] Y.S. Chung, T. Kim, T.H. Shin, H. Yoon, S. Park, N.M. Sammes, W.B. Kim, J. S. Chung, In situ preparation of a $La_{1.2}Sr_{0.8}Mn_{0.4}Fe_{0.6}O_4$ Ruddlesden–Popper phase with exsolved Fe nanoparticles as an anode for SOFCs, J. Mater. Chem. A 5 (2017) 6437–6446.
[60] H. Chang, E. Bjørgum, O. Mihai, J. Yang, H.L. Lein, T. Grande, S. Raaen, Y.-A. Zhu, A. Holmen, D. Chen, Effects of oxygen mobility in La–Fe-based perovskites on the

catalytic activity and selectivity of methane oxidation, ACS Catal. 10 (2020) 3707–3719.
[61] M. Sunding, K. Hadidi, S. Diplas, O. Løvvik, T. Norby, A. Gunnæs, XPS characterisation of in situ treated lanthanum oxide and hydroxide using tailored charge referencing and peak fitting procedures, J. Electron. Spectrosc. Relat. Phenom. 184 (2011) 399–409.
[62] C. Ramana, R. Vemuri, V. Kaichev, V. Kochubey, A. Saraev, V. Atuchin, X-ray photoelectron spectroscopy depth profiling of La_2O_3/Si thin films deposited by reactive magnetron sputtering, ACS Appl. Mater. Interfaces 3 (2011) 4370–4373.
[63] S. Mickevičius, S. Grebinskij, V. Bondarenka, B. Vengalis, K. Šliužienė, B. Orlowski, V. Osinniy, W. Drube, Investigation of epitaxial $LaNiO_{3-x}$ thin films by high-energy XPS, J. Alloys Compd. 423 (2006) 107–111.
[64] Y. Bu, Q. Zhong, D. Xu, W. Tan, Redox stability and sulfur resistance of $Sm_{0.9}Sr_{0.1}Cr_xFe_{1-x}O_{3-\delta}$ perovskite materials, J. Alloys Compd. 578 (2013) 60–66.
[65] S. Poulin, R. França, L. Moreau-Bélanger, E. Sacher, Confirmation of X-ray photoelectron spectroscopy peak attributions of nanoparticulate iron oxides, using symmetric peak component line shapes, J. Phys. Chem. C 114 (2010) 10711–10718.
[66] W.H. Kan, M. Chen, J.-S. Bae, B.-H. Kim, V. Thangadurai, Determination of Fe oxidation states in the B-site ordered perovskite-type $Ba_2Ca_{0.67}Fe_{0.33}NbO_{6-\delta}$ at the surface (nano-scale) and bulk by variable temperature XPS and TGA and their impact on electrochemical catalysis, J. Mater. Chem. A 2 (2014) 8736–8741.
[67] P.C. Graat, M.A. Somers, Simultaneous determination of composition and thickness of thin iron-oxide films from XPS Fe 2p spectra, Appl. Surf. Sci. 100 (1996) 36–40.
[68] J.S. Yoon, Y.-S. Lim, B.H. Choi, H.J. Hwang, Catalytic activity of perovskite-type doped $La_{0.08}Sr_{0.92}Ti_{1-x}M_xO_{3-\delta}$ (M= Mn, Fe, and Co) oxides for methane oxidation, Int. J. Hydrogen Energy 39 (2014) 7955–7962.
[69] S. Meiqing, Z. Zhen, C. Jiahao, S. Yugeng, W. Jun, W. Xinquan, Effects of calcium substitute in $LaMnO_3$ perovskites for NO catalytic oxidation, J. Rare Earths 31 (2013) 119–123.
[70] X.-Y. Long, J.-Y. Li, D. Sheng, H.-Z. Lian, Spinel-type manganese ferrite ($MnFe_2O_4$) microspheres: a novel affinity probe for selective and fast enrichment of phosphopeptides, Talanta 166 (2017) 36–45.
[71] M. Sunding, K. Hadidi, S. Diplas, O. Løvvik, T. Norby, A. Gunnæs, XPS characterisation of in situ treated lanthanum oxide and hydroxide using tailored charge referencing and peak fitting procedures, J. Electron. Spectrosc. Relat. Phenom. 184 (2011) 399–409.
[72] S. Mickevičius, S. Grebinskij, V. Bondarenka, B. Vengalis, K. Šliužienė, B. Orlowski, V. Osinniy, W. Drube, Investigation of epitaxial $LaNiO_{3-x}$ thin films by high-energy XPS, J. Alloys Compd. 423 (2006) 107–111.